Journal of Nuclear Materials 587 (2023) 154715

Contents lists available at ScienceDirect

Journal of Nuclear Materials

journal homepage: www.elsevier.com/locate/jnucmat

Precipitation of Cr-rich clusters in Fe-Cr alloys: Effects of irradiation from first principles modeling and experimental observations

Mark Fedorov [a], Jan S. Wróbel [a,*], Andrew J. London [b,c], Krzysztof J. Kurzydłowski [d], Chu-Chun Fu [e], Tonči Tadić [f], Sergei L. Dudarev [b,c], Duc Nguyen-Manh [b,c,*]

[a] Faculty of Materials Science and Engineering, Warsaw University of Technology, ul. Wołoska 141, 02-507 Warsaw, Poland
[b] CCFE, UK Atomic Energy Authority, Culham Science Centre, Abingdon, OX14 3DB, United Kingdom
[c] Department of Materials, University of Oxford, Oxford, OX1 3PH, United Kingdom
[d] Faculty of Mechanical Engineering, Białystok University of Technology, Poland
[e] Université Paris-Saclay, CEA, Service de recherche en Corrosion et Comportement des Matériaux, SRMP, F-91191 Gif-sur-Yvette, France
[f] Laboratory for ion beam interactions, Ruđer Bošković Institute, Bijenička 54, HR-10000 Zagreb, Croatia

GRAPHICAL ABSTRACT

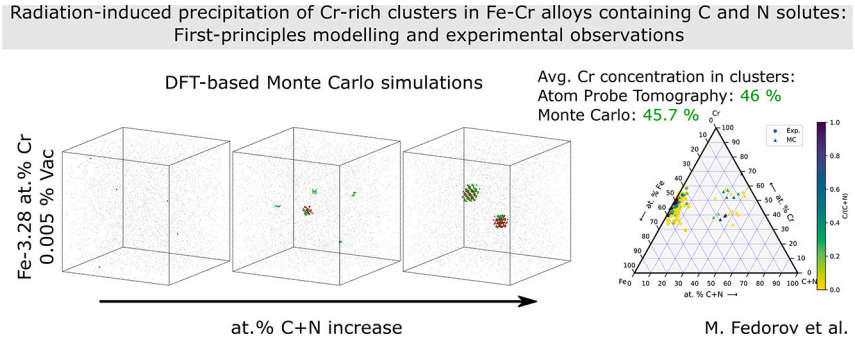

HIGHLIGHTS

- Cr-rich clusters are correlated with C and N in DFT-based modeling and experiments.
- The structure and composition of clusters vary with nominal % of C, N and vacancies.
- Cr concentration in the clusters is in quantitative agreement between MC and APT.

ARTICLE INFO

Keywords:
Irradiation effects
Fe Cr alloys
Density Functional Theory (DFT)
Cluster Expansion (CE)
Monte Carlo simulations

ABSTRACT

Using exchange Monte Carlo (MC) simulations based on an *ab initio*-parameterized Cluster Expansion (CE) model, we explore the phase stability of low-Cr Fe-Cr alloys as a function of vacancy (Vac), carbon, and nitrogen content. To parameterize the CE model, we perform Density Functional Theory calculations for more than 1600 supercells containing Cr-Vac-C-N clusters of various sizes in pure bcc Fe, Cr, and Fe-Cr alloys. MC simulations performed for $T = 650$ K show that Cr clustering in Fe-3.28 at.%Cr alloys does not occur if there are no defects or if only

* Corresponding authors.
E-mail addresses: mark.fedorov@pw.edu.pl (M. Fedorov), jan.wrobel@pw.edu.pl (J.S. Wróbel), andy.london@ukaea.uk (A.J. London), k.kurzydlowski@pb.edu.pl (K.J. Kurzydłowski), chuchun.fu@cea.fr (C.-C. Fu), tonci.tadic@irb.hr (T. Tadić), sergei.dudarev@ukaea.uk (S.L. Dudarev), duc.nguyen@ukaea.uk (D. Nguyen-Manh).

https://doi.org/10.1016/j.jnucmat.2023.154715
Received 7 March 2023; Received in revised form 1 September 2023; Accepted 3 September 2023
Available online 11 September 2023

Atom Probe Tomography (APT)

vacancies are present. But the addition of a small amount of C or N, at the level as low as 0.02 at.% in an alloy with no vacancies, routinely results in the formation of ordered compounds containing a high amount of Cr, C and N. Cr segregates to interstitial atoms and Cr content in such Cr-rich clusters increases as a function of C and/or N concentration. In the presence of vacancies, C/N aggregate to the core regions of vacancy clusters, making segregation of Cr-rich clusters less pronounced. The structure of Cr-rich clusters varies significantly, depending on the concentration of interstitial atoms and on the ratio of N to C. Predictions derived from MC simulations agree with experimental observations of Fe-Cr alloys exposed to ion irradiation. The concentration of Cr found in clusters containing C and N interstitial atoms is in qualitative agreement, and the absolute Cr content found in the clusters simulated at 650 K is in quantitative agreement with experimental Atom Probe Tomography (APT) observations of Fe-3.28 at.%Cr alloys irradiated at 623 K. The measured C and N content of 42±5 and 151±3 atomic ppm likely results from the contamination that occurred during ion beam irradiation.

1. Introduction

Ferritic-martensitic Fe-Cr-based alloys and steels, including EUROFER and ferritic ODS steels, are among the materials selected for DEMO first wall and structural applications [1]. EUROFER steel offers a good overall balance between mechanical properties, corrosion resistance and good stability under irradiation, exhibiting relatively low swelling [2,3]. However, these steels exhibit radiation hardening at low temperatures even at moderate radiation exposure. A possible reason for the loss of mechanical properties is the formation of precipitates of Cr-rich α'-phase [4–7] observed even in irradiated alloys with Cr concentration below the Cr solubility limit in Fe [8]. This effect appears to be associated with the radiation-driven clustering of chromium atoms, resulting in the formation of Cr-rich precipitates. The authors of Refs. [4,7,9] proposed that Cr precipitates were associated with dislocation loops. This suggestion was seemingly supported by the studies of crystallographic orientations of Cr clusters that appeared consistent with the habit planes of dislocation loops in bcc Fe-based alloys [7]. On the other hand, Haley et al. [5] observed that Cr-rich clusters in irradiated Fe-9%Cr alloys were consistently characterized by spherical or faceted geometry. This suggests that there might be another driving force, different from the elastic field of dislocation loops, responsible for the formation of Cr-rich clusters forming in the irradiated relatively dilute Fe-Cr alloys. According to the investigation of HCM12A and T91 alloys by Jiao et al. [9], there are competing sinks for Cr, including grain boundaries, phase interfaces, dislocations and inhomogeneously distributed ordered Cr phases. For the latter ones, the mechanism of formation may involve point defects.

Hypothetically, vacancies or interstitial atoms like carbon (C), nitrogen (N), or oxygen (O), might be responsible for Cr clustering. The very high concentration of vacancies in irradiated alloys stems from the generation of Frenkel pairs [10]. On the other hand, C, N or O atoms are always present in steels, either as alloying elements or as impurities. Recent Atom Probe Tomography (APT) experiments showed that impurities at concentrations as low as a few appm affect the structural evolution of alloys under irradiation. Kuksenko et al. [7] observed the co-segregation of Ni, Si and P in Cr-rich clusters in Fe-Cr alloys with Cr content varying in the interval from 2.5, 5, 9 to 12 at.%. Moreover, in Fe-2.5%Cr alloys, a higher concentration of C was found in Cr-rich clusters. Cr carbides were also observed in proton irradiated HCM12A alloy by Swenson et al. [11], whereas traces of nitrogen in the regions of Cr enrichment were detected in irradiated Fe-5%Cr alloys by Hardie et al. [4]. Authors of Ref. [12] also described the formation of carbides and nitrides in Fe-15%Cr alloys, but in a study of Fe-(3–18)%Cr set of alloys [13] they noted that clustering of Cr under irradiation occurred only if the Cr content exceeded 6%. Finally, Haley et al. [5] ruled out the possibility of the formation of chromium oxides in the clusters, as they observed no oxygen in the clusters.

This study focuses on the effect of C and N on the phase stability and microstructure of Fe-Cr alloys, which also contain a high amount of vacancies as a feature associated with irradiation.

Although the formation of Cr-rich phases in irradiated Fr-Cr alloys with low Cr content can be attributed to the interaction between radiation point defects, interstitial atoms and Cr atoms in the bcc Fe matrix, the exact nature of the processes responsible for the precipitation of Cr-rich phases remains unclear. Earlier theoretical studies performed using Density Functional Theory (DFT) showed that C, N and O strongly interact with vacancies, forming highly stable vacancy-solute clusters [14–17]. Vacancies give rise to the effective attraction between C or N that otherwise repel each other in pure bcc Fe matrix. Vacancies also attract Cr atoms [18] and together with C, they may form energetically stable Vac-Cr-C clusters [19]. However, it is not clear if these vacancy-mediated interactions can drive the segregation of Cr atoms in the bcc Fe matrix.

Multi-scale models for Fe-Cr alloys and compounds, treating atomic exchange [17], atomic-level kinetic [20,21] and object kinetic [22] Monte Carlo (MC) simulations, helped improve the understanding of structural stability of the alloys. However, the phase composition of Fe-Cr alloys is significantly modified by the presence of trace amounts of N and C, which would lead to formation of nitride and carbide phases in quaternary Fe-Cr-N-C system. Furthermore, neutron irradiation, apart from its kinetic effects, enriches the alloy with non-equilibrium vacancies.

In this study, we investigate the phase stability of Fe-3.28%Cr alloys containing vacancies, carbon and nitrogen. We use a combination of DFT, Cluster Expansion (CE) method and MC simulations, described in Section 2 of the paper, and perform experiments to validate our model, see Section 3. A similar theoretical approach was successful in explaining the anomalous segregation of Re and Os in irradiated dilute W-Re and W-Re-Os alloys [23,24]. The new Cluster Expansion lattice model for the Fe-Cr-Vac-C-N system introduces a second sublattice, in addition to the main bcc lattice, to describe the octahedral sites. The octahedral sites can be occupied by C or N. The various binding energies are analyzed in Section 4, whereas in the subsequent sections, we summarize the results of MC simulations (Section 5) and APT experiments (Section 6). Simulations and observations describing Fe-3.28%Cr alloys are compared in Section 7.

2. Computational methods

Fe-Cr alloys are important structural materials and are being investigated intensively by various experimental and theoretical techniques. Methods such as CALPHAD [25,26] allow one to investigate equilibrium phase diagram as a function of composition and accordingly estimate the solubility limits in the alloy. Apart from thermodynamic databases being developed for specific systems and new classes of systems [27,28], the methodology continuously evolves, with recent improvements in the description of alloys down to 0 K [29,30] and integration of DFT calculations [31–33]. According to CALPHAD calculations (see Fig. 1), for Fe-Cr alloys at 650 K there is a solubility limit at 7.35 wt.% Cr followed by a phase separation between the two BCC phases. However, the introduction of C and N in amounts as low as a fraction of ppm significantly modifies the Cr solubility.

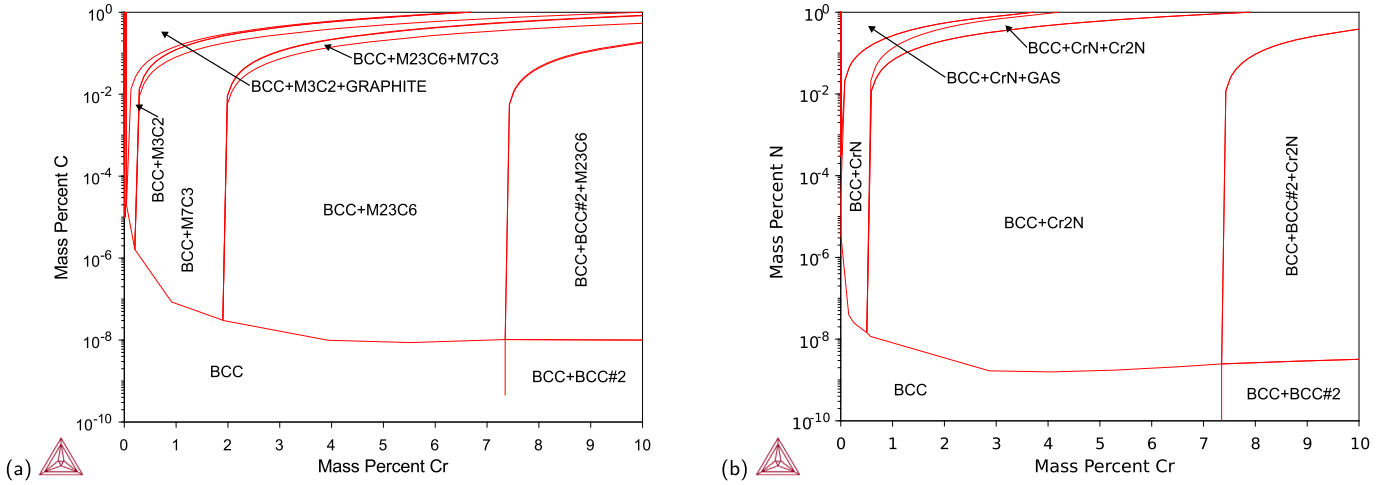

Fig. 1. Phase diagrams of (a) Fe-Cr-C and (b) Fe-Cr-N systems at 650 K, 1E5 Pa pressure, calculated using TCFE12 Thermo-Calc database in CALPHAD.

Table 1
Enthalpy of solution of interstitial C and N in a 128-atom supercell of Fe or Cr, as well as substitutional Cr in 127-atom supercell of Fe.

Structure	H_{sol}
1C in 128Cr	1.516
1N in 128Cr	-0.142
1C in 128Fe	0.760
1N in 128Fe	-0.241
1Cr in 127Fe	-0.132

The solubility in alloys can be understood by the analysis of the enthalpy of solution, H_{sol}, which is calculated as follows:

$$H_{sol} = E_{aM+bX} - aE_M - bE_X, \quad (1)$$

where E_{aM+bX} is the total energy of the matrix of M atoms with X solutes; a and b is the number of matrix and solute atoms, respectively; E_M and E_X are the reference energies of matrix and solute atoms, respectively.

As can be seen in Table 1, the solution enthalpy for C is positive in Fe, and more so in Cr, whereas for N it is negative in Fe and less so in Cr. The negative enthalpy for the solution of N implies that the formation of a solid solution of N in Fe is thermodynamically endothermic meaning that both Fe and Cr absorb N to form the energetically favorable product. Therefore there are no solubilities of N even at very low concentrations, which is consistent with the phase diagram, Fig. 1(b). The positive enthalpy of solution for C in Fe and Cr means that this process is exothermic implying C segregates from Fe or Cr even at small C concentration. This explains the solubility range of C in both Fe and Cr, in line with the phase diagram, Fig. 1(a). The enthalpy of solution for C in Fe is consistent with calculations from Ref. [34]. Enthalpy of solution for Cr in Fe is also negative, implying the formation of solid solution, which is consistent with recent CALPHAD evaluations of Fe-Cr phase diagram [35].

Irradiation of Fe-Cr-C-N alloy would introduce the non-equilibrium vacancies into the system, which affect phase stability of solid solutions and ordered phases present. In order to investigate the microstructure and phase stability on the atomic level, the application of relevant theoretical techniques is required.

2.1. Database construction

The constrained thermodynamic equilibrium of the Fe-Cr-Vac-C-N system as a function of composition, including the vacancy content and temperature, was investigated using a combination of Density Functional Theory (DFT), Cluster Expansion (CE) and Monte Carlo (MC) simulations. Such a methodology, applied earlier to W-Re-Vac alloys, explained the origin of clustering of Re atoms in irradiated W-Re and W-Re-Os alloys with low Re and Os content, see [23,24]. As an extension of these models, here the DFT-CE-MC methodology was applied to an alloy where atoms can occupy two different sublattices: (i) a sublattice of bcc sites, occupied by Fe or Cr atoms, or bcc vacancies, and (ii) a sublattice of octahedral sites, occupied by C or N atoms, or by the "octahedral lattice" vacancies. Vacancies on different sublattices are not interchangeable – for example, a bcc Vac is a real point defect on the bcc sublattice, whereas an octahedral Vac simply represents an unoccupied octahedral site. Fig. 2 shows a schematic view of the two sublattices, indicating the distances pertinent to the definition of the relevant binding energies.

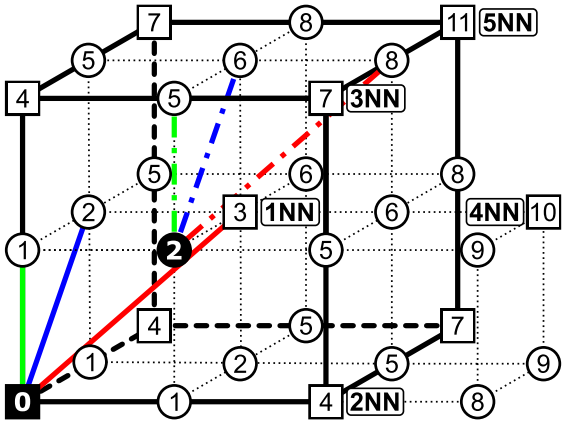

Fig. 2. Visualization of distances in a bcc unit cell: bcc lattice sites are shown as squares, and octahedral sites are shown as circles. Each site is characterized by its two-lattice nearest neighbor (nn) position with respect to the origin of the Cartesian coordinate system, situated at the bottom left corner of the diagram. Some of the sites (e.g. site 4) can only be occupied by atoms belonging to the bcc lattice. If the origin were chosen to reside on the octahedral lattice (e.g. on site 2 indicated by a solid circle), there would have been an asymmetry of a similar kind. Examples of the first three nn, involving pairs of sites on the two sublattices, are shown in identical colors – green, blue and red for the 1nn, 2nn and 3nn sites, respectively. Labels next to the bcc sites indicate distances given in the units of the bcc nearest neighbor distance (NN). (For interpretation of the colors in the figure(s), the reader is referred to the web version of this article.)

In the Fe-Cr-C-N system, there exist ground states which possess various lattices (see Table 2). It is worth emphasizing that all the stable structures predicted from this table are also present within the CAL-

Table 2
Formation enthalpies of the true ground states in Fe-Cr-C-N system. Structures marked with an asterisk (*) are not ground states and are provided for reference, which include cementite, fcc CrN stable at finite temperatures, as well as two structures included in our model (underlined): α-cementite and α-cementite-like Cr_3N, latter being the most stable structure in our model.

Structure	$Cr_{23}C_6$	Cr_7C_3	Cr_3C_2	Cr_2N	CrN	Fe_3N	FeN	CrN*	Fe_3C*	Fe_3C*	Cr_3N*
H_{form}	-0.074	-0.100	-0.099	-0.489	-0.680	-0.159	-0.295	-0.628	0.048	0.064	-0.322
Symmetry	$Fm\bar{3}m$	$P6_3mc$	Pnma	$P\bar{3}1m$	$P\bar{6}m2$	$P6_322$	$F\bar{4}3m$	$F\bar{4}3m$	Pnma	C12/c1	C12/c1

PHAD calculations seen in Fig. 1. In this work, we are focused on the formation of nano-sized clusters in the bcc Fe-Cr alloy. According to our experimental observations, discussed in Section 6, those clusters are semi-coherent to the bcc matrix. Additionally, the method intended to be used in this work can only consider one lattice (with multiple sublattices). Those facts motivated us to develop the model based only on the bcc lattice with a sublattice for interstitial defects. For comparison of H_{mix} of the experimental ground states with the structures that have been included in the model development, see Supplementary Material, Figs. S3, S4. It is of potential interest to investigate in future the formation of clusters of different phases shown in Table 2 which are more stable than the bcc phase.

To construct the CE model, DFT calculations were performed for the following groups of atomic structures:

1. Ordered Fe-Cr structures involving various primitive unit cells and a 2x2x2 conventional supercell, including the structures with interstitial clusters of C/N/C+N.
2. Clusters with Cr(Fe), Vac, N, C in bcc Fe(Cr) matrix in a 4x4x4 supercell. These include 2-, 3-, and 4-body clusters.
3. Compact 8-atom clusters of Cr atoms or vacancies (voids), defined using 4x4x4 and 5x5x5 supercells.
4. α-cementite-like structures – a prototype of a bcc precursor to iron carbide [36] – including the structures based on bcc 12-atom SQS Fe-Cr matrix and their derivatives, containing vacancies and various amounts of C and N. Fig. 3 provides a visual representation of this type of structures.

The full DFT database of Fe-Cr-Vac-C-N configurations used in this study comprises 1671 atomic structures.

DFT calculations were performed assuming collinear spin polarization and using the projector augmented wave (PAW) method implemented in VASP [37–42]. Exchange and correlation were treated in the generalized gradient GGA-PBE approximation [43]. The electron configurations of Fe, Cr, C and N ions in the PAW potentials were taken as $[Ar]3d^74s^1$, $[Ar]3d^54s^1$, $[He]2s^22p^2$, $[He]2s^22p^3$, respectively.

The total DFT energies of various structures were evaluated using a Γ-centered Monkhorst-Pack mesh [44] of k-points in the Brillouin zone, with the k-mesh spacing of 0.2 $Å^{-1}$. This corresponds to a 14x14x14 k-point mesh for a conventional bcc unit cell. The plane wave cutoff energy used in the calculations was 400 eV. The total energy convergence criterion was set to 10^{-6} eV/cell, and the force components relaxation cutoff was set to $5 \cdot 10^{-3}$ eV/Å.

The binding energies of defect clusters were assessed to verify if a clustered configuration were energetically favorable compared to separate defects, assuming various alloy configurations. The energies were computed as follows:

$$E_{bind}(a\cdot \mathrm{C},\ b\cdot \mathrm{N},\ c\cdot \mathrm{Vac},\ d\cdot \mathrm{Cr}) = a\cdot E_{tot}(1\cdot \mathrm{C}) + b\cdot E_{tot}(1\cdot \mathrm{N}) + c\cdot E_{tot}(1\cdot \mathrm{Vac}) + d\cdot E_{tot}(1\cdot \mathrm{Cr}) - E_{tot}(a\cdot \mathrm{C},\ b\cdot \mathrm{N},\ c\cdot \mathrm{Vac},\ d\cdot \mathrm{Cr}) - (a+b+c+d-1)\cdot E(\mathrm{Fe}) \quad (2)$$

where a is the number of C atoms, b is the number of N atoms, c is the number of vacancies, d is the number of Cr atoms in the Fe matrix. $E_{tot}(1\cdot C)$, $E_{tot}(1\cdot N)$, $E_{tot}(1\cdot Vac)$, $E_{tot}(1\cdot Cr)$ and $E_{tot}(a\cdot C,\ b\cdot N,\ c\cdot Vac,\ d\cdot Cr)$ are the total energies of Fe supercells containing one C atom, one N atom, one vacancy, one Cr atom and a cluster of these atoms, respectively. A positive value of the binding energy implies that defects attract each other and can form a cluster, whereas a negative value of E_{bind} indicates that the formation of a defect cluster is energetically not favorable and, if formed, such a cluster would decompose into separate individual point defects.

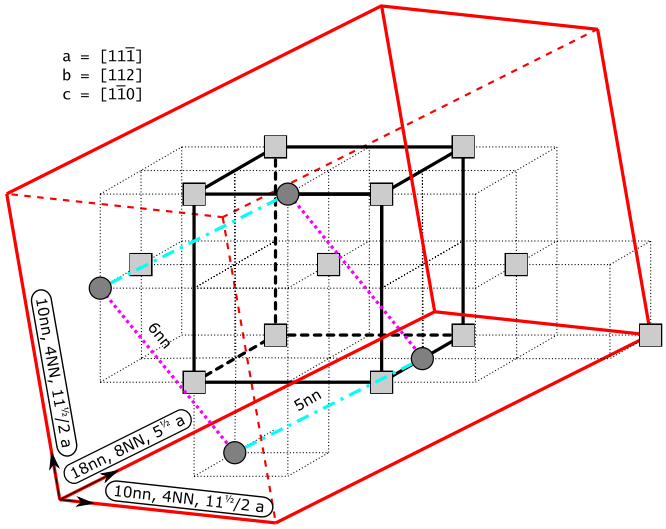

Fig. 3. Sketch of α-cementite, treated as a bcc precursor of the cementite phase. Bcc sites are shown as squares, whereas occupied octahedral sites are shown as circles. A black cube in the middle of the diagram represents a conventional bcc unit cell. The red parallelepiped represents an α-cementite primitive cell. Unit vectors of the primitive lattice are given in the nn, NN and lattice parameter (a) units. The shortest distance between a pair of two occupied octahedral sites is either 5nn (cyan dash-dotted lines) or 6nn (pink dotted lines). (For interpretation of the colors in the figure(s), the reader is referred to the web version of this article.)

2.2. Model construction and application

To assess the finite-temperature phase stability of a compound, it is necessary to first evaluate its stability at 0 K, defined by the enthalpy of mixing H_{mix}, and then develop a Cluster Expansion model and optimize the mapping of H_{mix} from DFT to CE to maximize the predictive capability of the model.

The enthalpy of mixing for a chosen alloy configuration, defined by a vector of configurational variables $\vec{\sigma}$ and evaluated using DFT, can be written as follows,

$$H_{mix}^{DFT}(\vec{\sigma}) = E_{tot}(\vec{\sigma}) - \sum_{p=1}^{K} c_p E_{tot}^{ref}(p), \quad (3)$$

where $E_{tot}(\vec{\sigma})$ is the total energy of the configuration, $E_{tot}^{ref}(p)$ is a reference energy corresponding to a pure component p, K is the number of alloy components and c_p is the average concentration of each component.

Once the values of H_{mix}^{DFT} were computed for all the structures included in the database, the structure inversion method was applied to

generate a CE parameterization. In the CE model, the enthalpy of mixing H_{mix}^{CE} is given by

$$H_{mix}^{CE} = \sum_{\omega,n,s} J_{\omega,n}^{(s)} m_{\omega,n}^{(s)} \left\langle \Gamma_{\omega,n}^{(s)}(\vec{\sigma}) \right\rangle . \tag{4}$$

Summation here is performed over all the clusters, distinct under symmetry operations in the two-sublattice model and described by the following parameters: ω is the number of lattice points ("bodies") in the cluster, n is the largest distance between two points in the cluster defined in terms of the nearest neighbor classification of the two-sublattice model (nn), and (s) is the decoration of the cluster, i.e. the occupation of the lattice points by atoms of a different kind in varying order. $J_{\omega,n}^{(s)} m_{\omega,n}^{(s)}$ is the effective cluster interaction in each cluster, $m_{\omega,n}^{(s)}$ is the site multiplicity of each cluster (in per-lattice-site units). $\left\langle \Gamma_{\omega,n}^{(s)}(\vec{\sigma}) \right\rangle$ are the so-called cluster functions, averaged over all the clusters with the same parameters.

A cluster function $\Gamma_{\omega,n}^{(s)}(\vec{\sigma})$ is a product of orthonormal point functions of occupation variables $\gamma_{j,K}(\sigma_i)$ for each cluster with the same ω and n,

$$\Gamma_{\omega,n}^{(s)}(\vec{\sigma}) = \gamma_{j_1,K}(\sigma_1)\gamma_{j_2,K}(\sigma_2)\ldots\gamma_{j_\omega,K}(\sigma_\omega). \tag{5}$$

Sequence $(s) = (j_1, j_2, \ldots, j_\omega)$ is the decoration of a cluster by point functions, where a point function is defined as

$$\gamma_{j,K}(\sigma_i) = \begin{cases} 1 & \text{if } j = 0\,, \\ -\cos\left(2\pi \left\lceil \frac{j}{2} \right\rceil \frac{\sigma_i}{K}\right) & \text{if } j > 0 \text{ and odd}, \\ -\sin\left(2\pi \left\lceil \frac{j}{2} \right\rceil \frac{\sigma_i}{K}\right) & \text{if } j > 0 \text{ and even}, \end{cases} \tag{6}$$

where $\sigma_i = i = 0, 1, 2, \ldots (K-1)$ is a number representing the constituent components of a K-component alloy, j is the index of point functions $j = 0, 1, 2, \ldots (K-1)$, and $\left\lceil \frac{j}{2} \right\rceil$ is the ceiling function that rounds up a rational number to the closest integer. In case of the multi-sublattice model, $\gamma_{j,K}(\sigma_i)$ can be calculated separately for each sublattice, and in such case, K is equal to the number of elemental species that can occupy the respective sublattice. In the current model, both sublattices are occupied by 3 elemental species (Fe, Cr, Vac on the bcc sublattice and C, N, Vac on the octahedral sublattice), thus two sets of point functions are identical.

It should be pointed out that octahedral "filler" vacancies are treated as separate atomic species and as such, they are included in the calculation of H_{mix}. Octahedral vacancies usually occupy the majority of the octahedral sublattice, which also translates to the majority of all occupied positions. Values of H_{mix} presented throughout this work, including Table 2 and Supplementary Material, Figs. S1–S4, are calculated using Eq. (3) without the consideration of octahedral "filler" vacancies. Reference states for elements in the investigated system are ferromagnetic bcc Fe, non-magnetic bcc Cr, graphite and N_2 molecule. The mapping of H_{mix}, derived from DFT calculations, to H_{mix} obtained from a CE model, parameterized using the structures included in the database, was performed using the ATAT package [45–48]. The CE method has been recently extended to include voids, decorated by transmutation products, in tungsten irradiated at high temperatures [23,24].

It should be noted that although the DFT calculations were performed with full optimization, including atomic coordinates, magnetic moments, cell volume and shape, and effective cluster interactions, applied in MC simulations, are assigned to ideal lattice sites which are fitted to the energies of fully relaxed structures, the displacements from the ideal lattice positions caused by the size and chemical composition variations are included implicitly via relaxed total energy calculations.

The predictive accuracy of a CE model can be quantitatively evaluated using the cross-validation score (CVS) [45]

$$CVS^2 = \frac{1}{N} \sum_{i=1}^{N} \left(E_{DFT}^{i} - E_{CE'}^{(i)} \right)^2 , \tag{7}$$

where $E_{CE'}^{(i)}$ is the energy of the i-th structure, predicted by fitting the CE energies to DFT energies, excluding E_{DFT}^{i} of the i-th structure.

Various sets of Effective Cluster Interactions (ECIs) were tested to find the best (minimum) CVS between the DFT and CE energies. The final set of ECIs includes pairwise interactions up to the third nearest-neighbor coordination shell in bcc lattice (53 interaction parameters) and 3-body interactions involving up to the second nearest-neighbor coordination shell in bcc lattice (114 interaction parameters).

Semi-canonical exchange MC simulations were performed using `memc2` subroutine of the ATAT package. Various supercell sizes have been tested, going up to 49x49x49 bcc unit cells, and a 37x37x37 supercell was selected as the optimal choice from the perspective of representability of the observed structures and the time cost. The optimal number of equilibration and accumulation Monte Carlo steps is 2000 per atom – this value has been used in all the MC simulations. For each composition, simulations were performed assuming a fixed temperature of 650 K, and starting from a disordered state.

2.3. DFT and CE model overview

Enthalpies of mixing from DFT calculations for the entire Fe-Cr-Vac-C-N database are illustrated in Supplementary Material, Fig. S1. Notably, the model is able to reproduce the region of Fe-rich structures characterized by negative H_{mix} (see Supplementary Material, Fig. S1(a)). By comparing the enthalpies of mixing of Fe-Cr structures without defects and those containing defects, we observe that the addition of the latter can drastically change H_{mix} and stabilize or destabilize the corresponding structures.

The enthalpies of formation of α-cementite-like $[Fe_xCr_y]_3[C_aN_b]$ structures, where x, y denote the concentration of the corresponding alloy components on the bcc sublattice, and a, b on the octahedral sublattice, are shown in Supplementary Material, Fig. S1(e,f,i). Influence of concentration of each element in the system on the stability of α-cementite-like phase (which is a potential bcc precursor of the cementite phase [36]) can be observed in these figures. Among the α-cementite-like structures, the lowest enthalpies of formation correspond to structures containing only nitrogen on the octahedral sublattice. All such structures have negative formation enthalpies. The least stable are the structures containing only C on the octahedral sublattice, and all of them have positive formation enthalpies. We also note that the enthalpies of formation of α-cementite-like phases decrease as a function of Cr content.

The values of effective cluster interaction parameters are given in Supplementary Material in Tables S2 and S3. The cross-validation score for the final mapping of H_{mix}^{DFT} to H_{mix}^{CE} is 5 meV. The fitted H_{mix} values of the Cluster Expansion model can be underestimated or overestimated in comparison with the DFT H_{mix}, as indicated by the difference between the values for respective structures, shown in the Supplementary Material, Fig. S2. In the case of some Fe-C structures, CE fitting produced negative values of H_{mix} (see Supplementary Material, Fig. S3(c)).

3. Materials and experimental methods

3.1. Materials and preparation

Ultra-high purity polycrystalline Fe-3wt.%Cr and Fe-5wt.%Cr alloys were produced by European Fusion Development Agreement (EFDA now EUROfusion) and manufactured by the École Nationale Supérieure des Mines (ARMINES) under contract EFDA-06-1901 [49]. Chemical analysis of the alloys in the as-received condition showed for one of the alloys 5.40 wt% Cr and in atomic ppm: C 4, S 3, O 6, N 2 and less than 5 P. The Fe3wt%Cr alloy contained 3.05wt% Cr and in atomic ppm: C 4, S 3, O 4, N 2 and <5 P. The specimens were cut (25x1x1 mm) by electrode discharge machining and surface damage removed using SiC abrasive paper of various grades, before polishing with 9 um and 1 um diamond paste followed by a chemo-mechanical polish using a suspension of colloidal silica (0.05 um).

3.2. Ion irradiation

Ion irradiation was performed at the laboratory for ion beam interactions in Ruđer Bošković Institute (RBI), Croatia. Both specimens were held using the thermal gradient holder which is described elsewhere [50]. A linear thermal gradient was imposed across the length of the specimen, resulting in a range of irradiation temperatures from 150 to 450 °C. Temperatures were monitored by two thermocouples embedded in one sample, and by thermal imaging. After the irradiation, the cold end and hot end edges were scored with a knife to mark the total irradiated area of 14.0×14.5 mm^2. The oval shaped heavy-ion beam (approx. 3 mm wide and 7 mm tall) was rastered over the irradiated area with the frequency of 488 Hz. The defined irradiation area was masked using aluminum plates to monitor the charge in-situ, and the masking was performed on the beam before an electron suppressed Faraday cup which was used to periodically check the beam current for the dosimetry of the exposures. Two irradiations with 4 MeV Fe^{2+} ions were performed, each totaling 3.0×10^{14} ions/cm^2, but one with a total time of 32,900 seconds and the other at a higher dose rate in 6840 seconds. This produced the peak damage of 0.3 dpa, and dose rates of 9.1×10^{-6} (low-dose rate, LDR) and 4.4×10^{-5} dpa/s (high-dose rate HDR). Damage calculations were carried out using SRIM-2013, assuming the threshold displacement energy of 40 eV and using the "simple" damage calculation method.

3.3. Atom Probe Tomography

A FEI (OR, USA) Helios NanoLab 600i focused ion beam (FIB) was used to prepare atom probe samples from the ion-irradiated material using the lift-out and place on silicon micro-post array method as described elsewhere [51]. Atom probe samples were prepared perpendicular to the surface between 200 and 300 nm in depth; this depth range corresponds to the irradiation damage dose of approximately 0.2 dpa.

Atom Probe Tomography was performed using a Cameca (Ametec, Madison USA) LEAP 5000 XR using a 355 nm UV laser and 52% detection efficiency. The pulse frequency was set to 200 kHz, laser pulse energy of 40 pJ and evaporation rate was kept at 0.005 detected ions per pulse by controlling the voltage. The specimen temperature was held at 50 K. Reconstruction of the atom probe data was performed using Imago Visualization and Analysis System (IVAS) [52], specifically IVAS 3.8.4, with the image compression factor of 1.5. The 0.20 nm spacing of the [110] crystallographic planes was calibrated by changing the initial tip radius in the voltage mode reconstruction method. The open source visualization software 3Depict (0.0.22) was also used for figures and axial distribution plots [53].

The maximum separation method (MSM) clustering algorithm [54] (IVAS 3.8.4) was used with Cr, C and N core ions. In general, a maximum separation, D_{max} of 0.5–0.6 nm with an order parameter [55] of 5 provided a good selection of the Cr-dense clusters. The increased order parameter avoided the low-density regions of C and N along the zone lines. A filter on the number of core ions detected was applied to reduce the chance of including clusters arising from random fluctuations. Depending on the data set, this varied between 35 and 150, to reduce the number of clusters occurring in a randomly mass-relabeled dataset to 100 times less than the number of clusters detected in the original data with the same settings [56]. The inclusion/envelope distance and the erosion distance were both set to half of the D_{max} value.

4. Binding energies of defect clusters

Binding energies of defect clusters of size up to 3 (e.g. 2Vac-1C) were analyzed as a part of assessment of phase stability of Fe-Cr-Vac-C-N alloys. Binding energies are calculated based on the results of fully optimized structures from DFT calculations. Since our model involves two sublattices, the smallest clusters may be defined either on the same sublattice, i.e. as a bcc-bcc defect cluster or as an octahedral-octahedral defect cluster, as well as an inter-sublattice bcc-octahedral defect cluster.

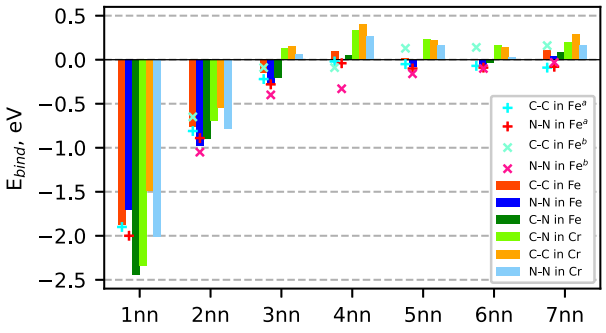

Fig. 4. Binding energies of C-C, N-N and C-N pairs in pure Fe and pure Cr from DFT calculations. Negative binding energy indicates repulsion. x-axis is the distance between two interstitial atoms in the bcc-octahedral two-sublattice model, illustrated in Fig. 2. Markers give comparison with earlier calculations by [a] Barouh et al. [17] and [b] Domain et al. [14].

4.1. Binding in 2-body clusters

4.1.1. Binding between interstitial atoms, and interstitial atoms and vacancies

To rationalize why the locations of the regions with higher Cr concentrations in Fe-Cr alloys observed experimentally correlate with the locations of higher concentrations of C and N, the binding energies of C-C, N-N and C-N interstitial two-body clusters in Cr and Fe matrices were investigated and compared with literature data.

Fig. 4 and Table 3 show that at smaller distances, the strength of repulsion between the interstitial atoms is high, corresponding to the large negative binding energy. Interaction between interstitial atoms weakens as the distance between them increases, in agreement with the data given in Refs. [14,17]. The binding energy for all the two-body clusters of interstitial atoms becomes positive in the Cr matrix starting from the 3nn distance, implying attraction, compared to the Fe matrix, where attraction starts from the 4nn distance. Interaction between interstitial atoms is stronger in Cr than in Fe. We also find that the N-N (nitrogen-nitrogen) interaction is always weaker compared to the C-C interaction, except for the case of a N-N pair in the Fe matrix at the 1nn distance. The smallest distances between the interstitial atoms in the $[Fe_xCr_y]_3[C_aN_b]$ structures are 5nn and 6nn, and the binding energies at those distances are positive in the Cr matrix, but are slightly negative or close to zero in the Fe matrix. This suggests that C and N may form $[Fe_xCr_y]_3[C_aN_b]$ clusters, and this trend is slightly stronger pronounced in the Cr matrix. The formation of structures with other types of ordering (e.g. with the shortest distances between interstitial atoms being 4nn and 7nn) might be more preferable.

4.1.2. Binding in the bcc sublattice

It is important to investigate how Cr atoms interact in a Fe matrix without any defects to see if Cr exhibits any tendency towards precipitation in the absence of C, N or vacancies. Fig. 5 shows that Cr atoms in the bcc Fe matrix repel each other, with repulsive interaction being the strongest at the 1NN distance, rapidly decreasing as a function of the distance between Cr atoms. At the 3NN distance, the interaction is eight times weaker than at the 1NN distance, still remaining repulsive. The values shown in Table 4 illustrate that the Cr-Cr interaction remains repulsive at the 5NN distance. This agrees with the data from Refs. [57,58].

Since vacancies form in abundance under irradiation, their effect on Cr clustering also warrants investigation. Two vacancies form what is known as a divacancy, referred to below as Vac-Vac. Vacancies bind at 1NN and 2NN distances in bcc Fe and Cr matrices and this binding quickly diminishes as a function of the distance between the vacancies,

Table 3
Binding energies from DFT calculations for C-C, N-N and C-N clusters in pure Fe and pure Cr. Distances are given in the notations of the bcc-octahedral two-sublattice model, illustrated in Fig. 2. Literature values from Barouh et al. [17] and Domain et al. [14] are also shown for comparison.

Dist. [nn]	2C in Fe [eV]	2N in Fe [eV]	CN in Fe [eV]	CN in Cr [eV]	2C in Cr [eV]	2N in Cr [eV]
1	-1.874 -1.9 [17]	-1.710 -2 [17]	-2.441	-2.345	-1.484	-2.014
2	-0.762 -0.81 [17] -0.65 [14]	-0.976 -0.89 [17] -1.05 [14]	-0.897	-0.693	-0.544	-0.784
3	-0.149 -0.22 [17] -0.09 [14]	-0.272 -0.28 [17] -0.4 [14]	-0.215	0.132	0.148	0.065
4	0.098 -0.02 [17] -0.09 [14]	-0.005 -0.04 [17] -0.33 [14]	0.049	0.331	0.403	0.264
5	0.019 -0.05 [17] 0.13 [14]	-0.077 -0.1 [17] -0.16 [14]	-0.004	0.237	0.220	0.168
6	-0.004 -0.07 [17] 0.14 [14]	-0.093 -0.09 [17] -0.1 [14]	-0.041	0.169	0.147	0.029
7	0.103 -0.09 [17] 0.16 [14]	0.045 -0.08 [17] -0.03 [14]	0.077	0.202	0.295	0.166

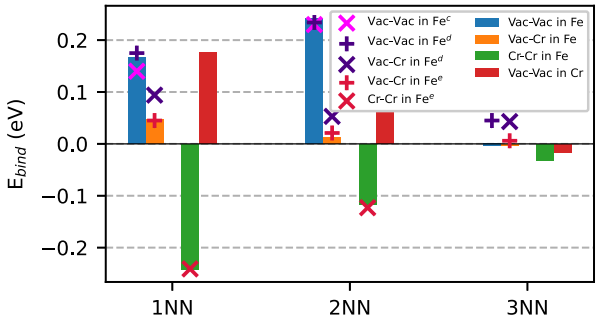

Fig. 5. Binding energies of Vac-Vac clusters in Fe and Cr from DFT calculations, shown together with the binding energies of Vac-Cr and Cr-Cr clusters in Fe from DFT calculations as a function of a distance between Cr atoms, in bcc nearest neighbor units. Literature values are taken from [c] Domain et al. [59], [d] Lavrentiev et al. [18], [e] Bakaev et al. [60].

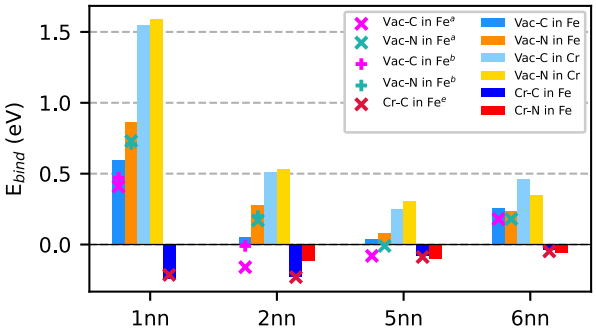

Fig. 6. Binding energies of Vac-C and Vac-N clusters in pure Fe and pure Cr from DFT calculations, and binding energies of Cr-C and Cr-N clusters in pure Fe from DFT calculations, shown as a function of the distance between a vacancy and an interstitial atom. At distances of 3nn, 4nn and 7nn there are no 2-body clusters involving atoms residing on different sublattices, hence such distances are not shown on the x-axis of the graph. Reference values are taken from [a] Barouh et al. [17], [b] Domain et al. [14], Bakaev et al. [60].

see Fig. 5. The binding between vacancies in bcc Fe is stronger than in bcc Cr, and this can make vacancies stay in the Fe-rich part of the lattice. In the bcc Fe matrix, the Vac-Vac binding energy is higher at 2NN than at 1NN distance, and this is reversed in bcc Cr. Moreover, the interaction between vacancies in Cr at the 3NN distance is repulsive. Vacancies bind to Cr much weaker than to each other (~ 0.05 eV versus ~ 0.18 eV), and at the 3NN distance Vac-Cr clusters already start exhibiting slight repulsion, see Fig. 5. This suggests that vacancies are not expected to facilitate clustering of Cr and instead, the evolution of vacancies gives rise to the formation of vacancy clusters or voids. Binding energies of Vac-Vac, Vac-Cr and Cr-Cr clusters are generally in agreement with the literature values taken from Refs. [59,60,18], see Table 4.

4.1.3. Binding of interstitial atoms to vacancies

We now consider the interaction between interstitial C and N atoms with vacancies. Vac-C and Vac-N clusters form bound configurations in Fe and Cr matrices, with stronger attraction found in Cr, see Fig. 6 and Table 5. This agrees with the analysis performed in [17,14]. Vac-N binding is always stronger than binding in Vac-C except for the case of the 6nn configuration. The energy of binding between a vacancy and an interstitial atom is minimum at the 5nn distance.

Binding energies computed for the C-C, N-N, Vac-C and Vac-N clusters are generally in agreement with literature data [17,21].

Fig. 6 also shows the binding energies of Cr-C and Cr-N configurations. All the binding energies are negative, indicating repulsion; at the 1nn and 2nn distances, Cr-N binding is less negative compared to Cr-C, and at the 5nn and 6nn distances, the sign is reversed. The data on Cr-C binding agree very well with the data published in Ref. [60].

4.2. Binding in 3-body clusters

Since 3-body interactions are taken into account in our CE model, it is necessary to analyze the binding energies of 3-body defect clusters, more specifically, mixed bcc-oct clusters.

Table 4
Binding energies from DFT calculations for two-body interstitial defect clusters in Fe and Cr as a function of the distance between the atoms, expressed in bcc nearest neighbor units. Literature values are from Domain et al. [59], Bakaev et al. [60], and Lavrentiev et al. [18].

Distance [NN]	Vac-Vac in Cr [eV]	Vac-Vac in Fe [eV]	Vac-Fe in Cr [eV]	Vac-Cr in Fe [eV]	Fe-Fe in Cr [eV]	Cr-Cr in Fe [eV]
1	0.176	0.166 0.14 [59] 0.175 [18]	-0.870	0.047 0.045 [60] 0.094 [18]	-1.122	-0.242 -0.241 [60]
2	0.066	0.242 0.23 [59] 0.234 [18]	-1.008	0.013 0.021 [60] 0.053 [18]	-1.407	-0.117 -0.123 [60]
3	-0.017	-0.004 0.045 [18]	-1.074	-0.003 0.006 [60] 0.043 [18]	-1.287	-0.032
4	-0.808	0.064 0.055 [18]	-1.133	-0.011 -0.016 [60] -0.01 [18]	-1.439	-0.034
5	-0.913	0.071	-1.052	0.028 -0.001 [18]	-1.264	-0.033

Table 5
Binding energies of Vac-C and Vac-N clusters in pure Fe and pure Cr from DFT calculations shown as a function of the distance between a vacancy and an interstitial atom. Literature values are taken from Barouh et al. [17], Bakaev et al. [60], Domain et al. [14].

Distance [nn]	Vac-C in Fe [eV]	Vac-N in Fe [eV]	Vac-C in Cr [eV]	Vac-N in Cr [eV]	Cr-C in Fe [eV]	Cr-N in Fe [eV]
1	0.598 0.41 [17] 0.47 [14]	0.866 0.73 [17] 0.71 [14]	1.551	1.592	-0.241 -0.214 [60]	0.006
2	0.053 -0.16 [17] -0.01 [14]	0.276 0.17 [17] 0.2 [14]	0.515	0.532	-0.228 -0.23 [60]	-0.114
5	0.039 -0.08 [17]	0.084 -0.01 [17]	0.247	0.307	-0.079 -0.088 [60]	-0.103
6	0.257 0.18 [17]	0.238 0.18 [17]	0.460	0.350	-0.042 -0.048 [60]	-0.056
8	-0.031 -0.04 [17]	-0.049 -0.06 [17]	0.063	0.041	-0.028 -0.046 [60]	-0.037
9	-0.022	-0.007	0.022	0.021	-0.022	-0.028

4.2.1. Binding of two interstitial atoms to a vacancy

Defect clusters involving one vacancy and two interstitial atoms, carbon or nitrogen, bind together when the distance between the interstitial atoms is larger than their distances to a vacancy. They exhibit repulsion when the distance between the interstitial atoms is smaller or equal to the distance between them and the vacancy, see Fig. 7. The notations used for the horizontal axis in Fig. 7 are as follows: the first two digits in a label give information about the distance between a vacancy and each interstitial atom, the third digit is the distance between the interstitial atoms. 112 configuration corresponds to a C-C dimer shown in Ref. [61], Fig. 5(d), and 114 configuration corresponds to a C-C dimer shown in Ref. [61] Fig. 5(a) and Ref. [62] Fig. 2(d).

For the case of a Vac-CN, there are configurations where either C or N is closer to a vacancy. The difference between the binding energies of such clusters is quite small and only a cluster with higher E_{bind} is shown in the figure. Binding energies derived from our calculations are in agreement with literature data [14,19].

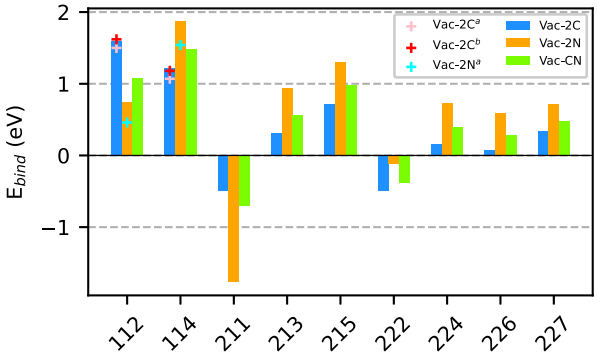

Fig. 7. Binding energies of clusters containing one vacancy and two interstitial atoms in Fe from DFT calculations. The notations on the horizontal axis are as follows: the first two digits in a label represent the distance between each interstitial atom and a vacancy, and the third digit refers to the distance between the interstitial atoms. For example, a 112 configuration corresponds to the occupied sites 0,1,1 in Fig. 2. Reference values are taken from [a] Domain et al. [14] and [b] Bonny et al, [19].

4.2.2. Binding of 2 vacancies to an interstitial atom

A number of 3-body clusters involving 2Vac and C or N, considered by Barouh et al. [17] in the context of bcc Fe matrix, were also explored for bcc Cr. The binding energies computed for those clusters are shown in Fig. 8. The magnitude of attraction is higher in a 2Vac-1N cluster

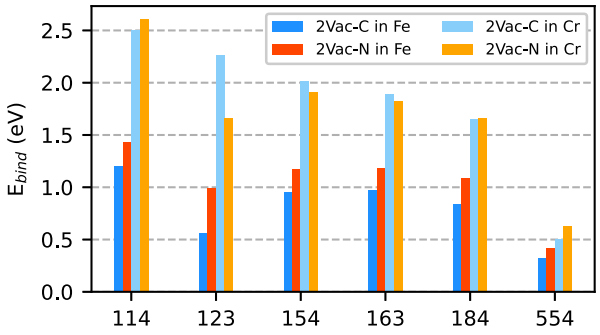

Fig. 8. Binding energies of 2Vac-C and 2Vac-N clusters in pure Fe and pure Cr from DFT calculations. The notations are as follows: the first two digits in a label give information about the distance between each vacancy and the interstitial atom, and the third digit refers to the Vac-Vac distance.

than in a 2Vac-1C cluster in the bcc Fe environment. In bcc Cr, there is no clear difference between the two types of clusters, but for both cases, the binding is stronger compared to their counterparts in bcc Fe. Similarly to the case of the two-body vacancy-interstitial clusters, the positive binding energies of the clusters might be responsible for the formation of 2Vac-C/N clusters in Fe-Cr-Vac-C-N alloys, with a possible slight preference for them forming in the Cr-enriched regions.

4.3. Overview of binding energies

From the analysis of binding energies above, we observe that interstitial atoms attract at large distances but prefer not to stay too close to each other. This type of interaction favors the formation of structures with increased yet relatively disperse distribution of interstitial atoms, for example, ordered phases similar to $[Fe_xCr_y]_3[C_aN_b]$ structures. The addition of vacancies may modify the behavior of interstitials, and the strong attraction between vacancies and interstitials may overcome the repulsion of interstitials at short distances, promoting the segregation of interstitial atoms to vacancies. Since vacancies attract each other at nearest and next-nearest neighbor distances, the above pattern of interaction favors the formation of voids surrounded by carbon and nitrogen atmospheres.

Cr-Cr repulsion is stronger than Cr-Vac attraction. Cr-interstitial clusters also have negative binding energies, i.e. Cr solute atoms and interstitial atoms repel each other, resulting in that the formation of Cr-C/N clusters appears unlikely. We note that this does not agree with the earlier analysis of $[Fe_xCr_y]_3[C_aN_b]$ structures, suggesting that $Cr_3[C_aN_b]$ structures have negative formation energy and hence are expected to be stable. This contradiction may be explained by the fact that the two observations involved different choices of the reference environment: binding in 2-atom clusters was investigated in pure metals, whereas the analysis of $[Fe_xCr_y]_3[C_aN_b]$ structures spans mixed matrices and significantly higher concentrations of interstitial atoms.

5. Monte Carlo simulations

Interactions in a Fe-Cr-Vac-C-N alloy are complex and vary significantly, depending on the local composition of the alloy. To explore the effects of segregation in irradiated Fe-Cr alloys, we performed MC simulations of Fe-Cr-Vac-C-N alloys containing 3.28 at.% Cr at 650 K. This corresponds to the alloy composition and irradiation temperature used for the experimental observations described in Section 3. MC simulations assess the thermodynamic equilibrium state of an alloy at a given temperature.

Since we are working with the on-lattice simulations of a solid solution of atomic species (as opposed to molecular species), we choose to indicate the concentration of any element in atomic percents, which in this context are equivalent to molar %. If not stated otherwise, in the following text, the percentage related to the concentration of atomic species implies at.%.

In what follows, we explore the effect of interstitial C and N atoms as well as vacancies on the microstructure of Fe-Cr alloys.

5.1. The role of interstitial atoms in alloys without vacancies

It should be noted immediately that in an alloy without irradiation damage at temperatures around $0.3T_m$, the equilibrium concentration of vacancies is negligibly small and would require unreasonably large supercells to simulate. The smallest possible concentration of vacancies in the simulation cells chosen by the authors of this work is 1×10^{-5}, hence any vacancy concentration considered is non-equilibrium. As such, the simulation cell representing an alloy without non-equilibrium vacancies has no vacancies at all.

The effect of C and N interstitial atoms on the microstructure of Fe-Cr-C-N alloys containing no vacancies is shown in Fig. 9(a). In an alloy containing no C and N (see the left panel in Fig. 9(a)), the Cr atoms, shown as gray points, are uniformly distributed over the lattice, in agreement with earlier theoretical and experimental studies [57,63].

If C and N interstitial atoms are present in the system, usually they are not distributed randomly throughout a supercell but form locally ordered phases, starting from concentrations as small as 0.02 at.% (see Fig. 9(a), middle and right panels). The types of clusters most frequently observed for equal concentrations of C and N in an alloy without vacancies are shown in Fig. 10(g) and Fig. 10(h). These are the locally ordered Fe-Cr-N-C and Fe-Cr-N clusters, respectively. The ratio of Cr to Fe content in such clusters may vary, but generally with increasing concentration of C and/or N in a cluster, the concentration of Fe in a cluster decreases and the concentration of Cr increases for both types of clusters shown in Fig. 10(g) and (h). The concentration of Cr is higher on average in clusters of type Fig. 10(h), which contain more N compared to the clusters shown in Fig. 10(g).

In clusters of type Fig. 10(g), C and N prefer grouping with interstitial atoms of the same type on the interstitial sublattice. This results either in the formation of a cluster that is an agglomerate of two parts, each containing a high concentration of either C or N (as seen in Fig. 10(g)), or, more rarely, in the formation of a cluster where one interstitial type aggregates in the inner part, and the other interstitial in the outer part of the cluster. Fe atoms are observed more often in the C-rich part of the cluster. In clusters shown in Fig. 10(h), Fe atoms are observed only at clusters' boundaries.

5.2. The role of vacancies

The effect of vacancies on the microstructure of Fe-Cr-C-N alloys is illustrated in Fig. 9(b). The concentration of vacancies in the structures generated using MC simulations was 0.005 at.%.

First, we note that vacancies do not form clusters in Fe-3.28%Cr alloy at 650 K if there are no interstitial atoms present in the material (see the top left panel in Fig. 9(b)).

The effect of vacancies on the clustering of interstitial atoms is noticeable and is different for C and N interstitials. Nitrogen prefers to occupy the nearest neighborhood of any amount of vacancies, even one, which leads to the formation of multiple such defect clusters in the simulated cell (see Fig. 9(b) middle left). This type of cluster, shown in Fig. 10(a), is the smallest one observed in all the Monte Carlo simulations.

At higher N concentrations (Fig. 9(b), bottom left), the defects aggregate together and form larger clusters containing N and vacancies (Fig. 10(b)) observed in smaller numbers in the supercell, compared to the lower N content.

Carbon does not form small clusters and instead usually forms a single larger cluster of the type shown in Fig. 10(c) in the simulated cell, which increases in size with increasing C concentration (see Fig. 9(b) top row).

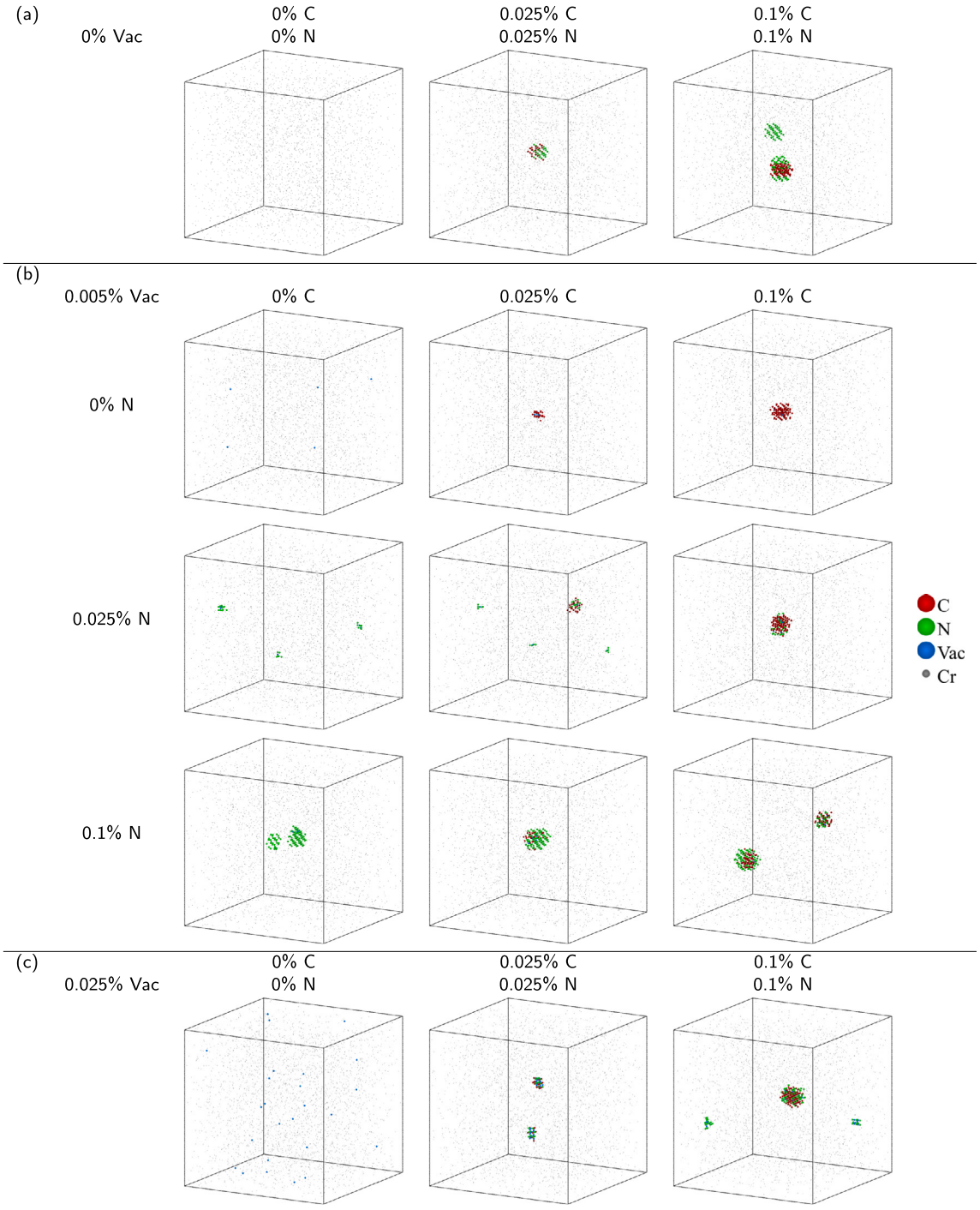

Fig. 9. Snapshots taken from Monte Carlo simulations of Fe-3.28%Cr at 650 K with different nominal concentrations of C and N, as well as vacancy concentrations being (a) 0%, (b) 0.005% and (c) 0.025%.

For the same nominal concentrations of C and N, when their total concentration does not exceed approximately ten times the vacancies concentration (Fig. 9(b) center), there is occasional occurrence of the smallest Vac-N clusters of the type shown in Fig. 10(a) and a new type of cluster, a mixed C-N-Vac type with C concentration being slightly higher than N, shown in Fig. 10(e). All the C atoms in a supercell belong to this type of cluster at the nominal composition corresponding to Fig. 9(b), center.

As the C+N concentration increases above ten times that of vacancies, only the clusters of type Fig. 10(e) are observed in the lattice, with multiple clusters exhibiting high C+N concentration (see Fig. 9, bottom right).

5.3. *Effect of higher vacancy content*

The microstructure of Fe-3.28%Cr alloys containing both C and N and a higher concentration of vacancies, namely 0.025%, is shown in Fig. 9(c). In supercells without C or N, the vacancies are distributed uniformly in the lattice, see Fig. 9(c), left panel.

For the concentration of C+N two times higher than that of vacancies (Fig. 9(c), middle), we observe predominantly the clusters of the

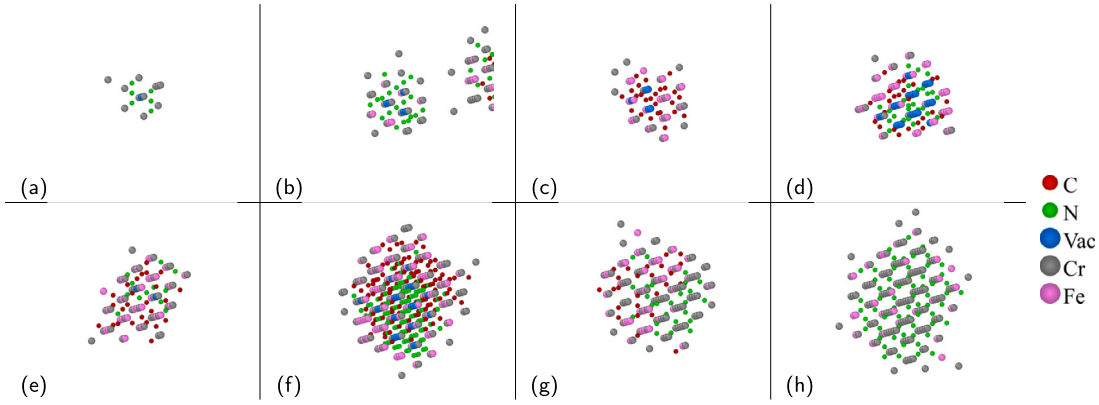

Fig. 10. Most observed clusters in compositions presented in Fig. 9, which are various combinations of vacancy concentration equal to 0, 0.005 and 0.025 % and concentration of C and N equal to 0, 0.025 and 0.1 %. The average size increases from (a) to (h).

type shown in Fig. 10(d). This clusters type is similar to that shown in Fig. 10(e) in that it has all the elements present in the system, however, Fig. 10(d) type has Vac and Fe dominantly on the bcc sublattice instead of Cr, which dominates in the Fig. 10(e) type of clusters.

Since the interstitial sublattice has three times more positions than the bcc sublattice, this may be assumed as a theoretical threshold value in MC simulations when the interstitial sublattice part of the bcc Vac cluster is completely filled with C and/or N. Below this limit, the interstitials can be described as situated inside a void. It should be noted that since the MC simulation model used in this study uses a rigid lattice, the actual distorted configuration of a defect cluster with C and/or N located inside the void remains effectively unknown. In a real alloy, the formation of C+Vac clusters might result in the precipitation of graphite, whereas N+Vac clusters probably form gas bubbles, i.e. small voids filled with N_2 molecules.

In Fig. 9(c), right panel, the ratio of C+N to Vac is higher than the aforementioned threshold value, which leads to the occurrence of clusters of type Fig. 10(f), where the concentration of Cr, although not being dominant, is higher compared to the nominal Cr concentration. C atoms are mostly found in those types of clusters, and N can also be found in multiple small clusters of type Fig. 10(b) throughout the simulation cell.

It should be mentioned that the voids containing no interstitial atoms have been observed only in the simulations where nominal vacancy concentration was approaching or was higher than 0.1%, hence resembling a material exposed to a high dose of irradiation [10,64]. In the great majority of simulations with such Vac concentrations, the vacancies were mostly distributed uniformly in the supercell.

5.4. Summary of Cr clustering versus C, N and vacancy concentrations

Fig. 11 presents an analysis of Cr concentration around interstitial defects. The maximum separation distance for the detection of clusters, where concentrations were measured, is the same as in APT and MC analysis and is equal to 0.4 nm. Due to the lattice nature of MC simulations, the maximum separation distance there is effectively limited to 0.347 nm = 6nn = 2NN – the largest bcc-oct distance considered in the model.

Fig. 11 shows that there is a strong correlation of Cr concentration around interstitial defects with both the concentration of vacancies and interstitial defects themselves, although the correlation has a different sign. For any concentration of vacancies, the Cr concentration increases with the increase of C+N concentration – Cr tends to precipitate around the interstitial defects. The largest concentrations are observed when there are no vacancies in the alloy and the concentration of interstitials is as low as 0.01%. When vacancies are added to the alloy, Cr concentration around the defects decreases, and this reduction is more pronounced at higher vacancy concentrations. This is caused by the formation of voids and aggregation of C/N interstitials inside these voids

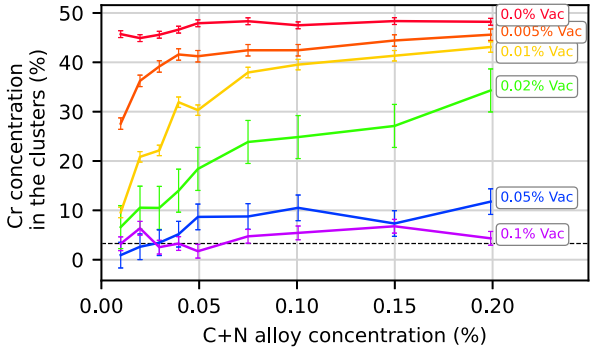

Fig. 11. Concentration of Cr in Cr-C-N-enriched clusters at 650 K as a function of nominal concentration of C and N. Concentrations of C and N are equal, %C = %N = %(C+N)/2. Series represent different nominal concentrations of vacancies in the alloy. The concentration of Cr in clusters is calculated using the method of maximum separation distance with the following parameters: $d_{max} = d_{bulk} = d_{erode} = 0.4$ nm, $n_{min} = 10$. All the data points in the series represent values averaged over 10 simulations with identical parameters (temperature, compositions, number of accumulation and equilibration steps), starting from different random initial positions of atoms. Error bars around each point show confidence intervals with $\alpha = 0.95$. The dashed line indicates the nominal concentration of Cr in all simulations, 3.28 at.%.

instead of them getting involved in the formation of ordered phases with Cr. As can be seen in the figure, the concentration of Cr does not exceed the nominal concentration when %Vac = %C+N. To make sure that the observed increased Cr concentration is not caused by a choice of the cutoff distance, a larger cutoff of 0.53 nm = 14nn = 6NN has been tested and the increased concentration of Cr around interstitial defects was still observed, with the effect being on average 5% smaller compared to the 6nn cutoff.

The general trend of Cr-composition with C-N-Vac content can be seen in more detail in Supplementary material [65] in Figs. S5 and S6, confirming that N has a stronger effect on precipitation of Cr-rich clusters compared to C discussed in this section.

6. Experimental results from APT

Atom Probe Tomography revealed a high number density of Cr-rich clusters in the Fe-3.28at%Cr material ion irradiated at both high and low dose rates to peak damage of 0.3 dpa at 623±25 K. Fig. 12 shows a representative 65x65x65 nm^3 volume with the clusters which have been detected isolated. Across all samples, the mean cluster number density was 2.4–6.3×10^{22} clusters per m^3 (95% confidence interval, CI95%), as defined by the cluster selection parameters given in the methods section.

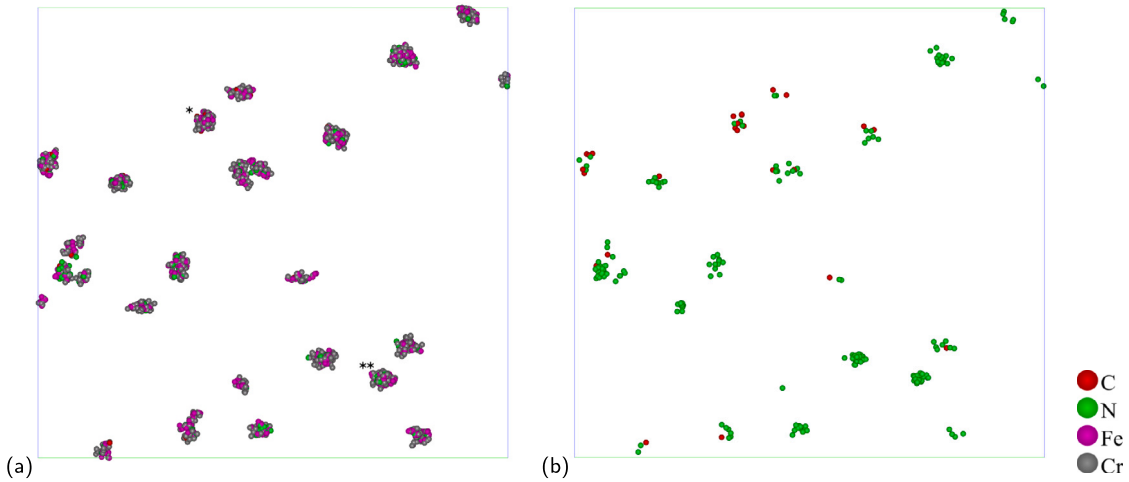

Fig. 12. Clusters in experimental data isolated from their surroundings in Fe-3.28%Cr alloy irradiated to 0.2 dpa at 623±25 K. A variation in C and N content is observed. The figure size is 65x65 nm. (a) showing Fe, Cr, C and N, (b) showing only C and N. Average cluster composition: Fe-50.4 Cr-44.1 N-4.7 C-0.7 at%. * and ** indicate clusters shown in detail in Fig. 15.

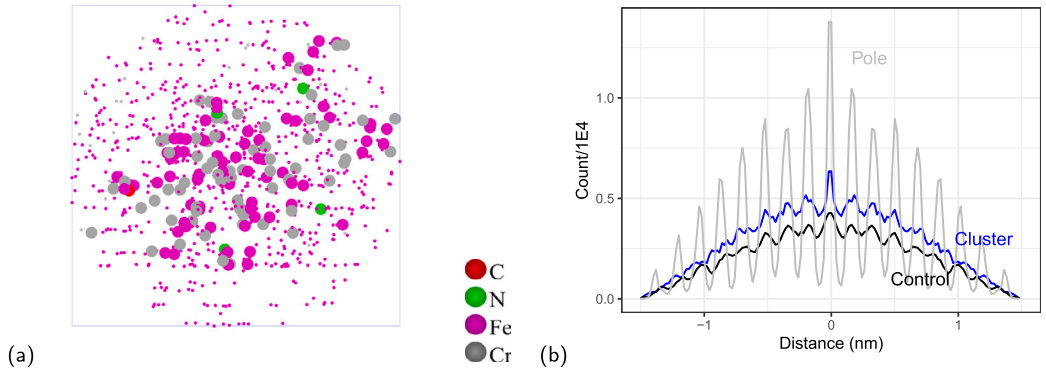

Fig. 13. (a) A 3 nm diameter spherical volume containing a cluster from the Fe-3.28%Cr alloy irradiated to 0.2 dpa near the [002] pole in reconstructed atom probe data. The atoms identified as part of the cluster are shown with a larger size. The histogram of relative atomic positions is shown in (b) for the volume in (a) "Cluster", a volume at the [002] "Pole" and a volume the same distance from the pole called "Control". In all cases, the volume was rotated so the planes were parallel to the analysis direction. A plane spacing of approximately 0.14 nm is visible in each.

Note that these Cr-rich regions, shown in Fig. 12a, also correlate with increased C and N contents, shown separately in Fig. 12b. The initial C and N content is very low, less than 8 ppm in total, however in the irradiated samples the measured content of C and N was 42±5 and 151±3 atomic ppm (8 experiments totaling 116 million ranged ions, 2 volumes with excess C near the original tip surface were excluded). The excess solute measured is likely to be the result of contamination from the ion beam irradiation, which is commonly observed [66].

In the reflectron atom probe, atomic planes are only resolved where the planes are perpendicular to the evaporation surface. To investigate the coherency of the Cr-rich clusters, clusters were selected that were near the pole regions identified from the ion hit map in the atom probe reconstruction. One such example from near the [002] pole in one sample is shown in Fig. 13. In Fig. 13(b) a histogram of the relative atomic positions is used to show if any atomic planes are present. The weaker signal from the planes shown by the cluster and control regions in Fig. 13(b) is due to not being from a slightly different position from the pole where the planes are not exactly parallel to the evaporation surface. Several clusters were observed as being coherent along the [110] direction and so it is expected that these clusters are at least semi-coherent with the BCC lattice.

The atom probe data have been reconstructed to give accurate plane spacings in the matrix, however, there is evidence of trajectory aberrations in the vicinity of the clusters which makes direct measurement of their size uncertain. This effect may explain the difference in cluster morphology shown in Fig. 15. Measuring the cluster diameter parallel to the analysis direction should give the most reliable measurement [67], and this was measured as 2.7–3.1 nm CI95%.

To give a reproducible indication of size irrespective of reconstruction parameters, the excess Cr ions can be counted using the "matrix correction" described in Ref. [56]. Excess ions are measured after removing all the Fe ions and the corresponding proportion of Cr according to the expected matrix composition. The clusters had a detected range of excess Cr ions between 100 and 130 (CI95%). A known fraction of ions is lost in the evaporation and detection process, however after correcting for the detector efficiency, the clusters are expected to contain 190–250 excess Cr ions (CI95%).

The composition results from the maximum separation method, with no mass-peak overlap solving or background subtraction, give the average composition of individual clusters. The 95% confidence interval for the cluster composition was Fe 50.5–51.9%, Cr 45.2–46.8%, C 0.24–0.38% and N 2.0–2.8% all in atomic percent.

To test the reliability of the cluster selection parameters, the variability of reported results was investigated with a range of D_{max} values. Analysis of the same data set with similar D_{max} values of 0.50, 0.55 and 0.60, with the inclusion and erosion distances set to $D_{max}/2$, gave Cr fractions in the clusters of 0.48, 0.47 and 0.45 all with approximately ±0.05 95% confidence intervals. While the clusters identified did not change, their apparent concentration is somewhat sensitive to the inclusion and erosion parameters selected.

The analysis of the Cr-rich clusters by atom probe is complicated by a number of factors. These are broadly separated into two groups relating to the spatial location of ions and to the measured composition. The small size of the clusters, containing only a few hundred excess Cr ions, is approaching the limit of what can be reliably separated using cluster detection. This will increase the subjectivity of the analysis and the accuracy of the measured composition.

The increased reconstructed density in the vicinity of the clusters is evidence of some de-magnification during evaporation and the resulting trajectory aberrations will reduce the accuracy of the spatial reconstruction, thus impacting the selection of the clusters.

Without other supporting evidence, it is not possible to tell reliably using an atom probe what fraction of Fe is a true component of the clusters and that which is included by the cluster selection and trajectory aberrations. From looking at a range of reasonable cluster selection parameters, it is judged that the Cr fraction is in the range of 0.3 to 0.6.

Turning to the C and N concentrations in the clusters, these are also likely to be effected by several artefacts which reduce the measured content of interstitial atoms. Thermally activated surface migration of some species is enhanced by the electric field and may cause C and N to migrate from the clusters before evaporating [68]. There is some evidence of the mobility of these ions from the clusters by looking at volumes of the data with and without clusters. Volumes with clusters, but with the clustered ions removed, showed an 80% increased content of C and N, from 70±40 to 120±40 and from 130±20 to 230±30 atomic ppm respectively, as compared to a volume which did not contain any detected clusters. This increase in solute in the region surrounding the clusters suggests some migration of these ions from the clusters meaning they are not included in the cluster selection and subsequent measurement. Based on the concentration of C and N, in volume around the clusters contained 125 extra C ions and 230 extra N ions, compared to 19 C ions and 35 N ions detected in the clusters themselves. C and N are either lost from the cluster or there is extra C and N near where the clusters are formed because of other microstructural features like dislocations.

Using the cluster radial concentration profile in IVAS the Cr concentration was enhanced to a distance of 2–2.5 nm from the cluster center but the C and N concentration was increased up to a distance of 4–6 nm. The composition of a radius of 6 nm around the cluster centers (with the cluster ions removed) had an increased C and N content of $40 < C = 100 < 170$ and $260 < N = 320 < 380$ compared to $10 < C = 17 < 26$ and $89 < N = 97 < 103$ atomic ppm in the remainder of the analysis volume more than 6 nm from any cluster. In these 6 nm radius spheres, this is an excess of 75 C atoms and 204 N atoms, after background subtraction and correcting for detection efficiency, compared to 19 C and 244 N atoms detected as part of the cluster selection. If these excess solute atoms all are associated with the clusters, it means that the clusters only account for 20% of the C and 45% of the N solute atoms which are actually increased in the region of the clusters. To "correct" the solute content of the cluster composition by MSM the C content would be multiplied by 5 and the N content doubled, with other loss mechanisms ignored.

The atom probe data measurements show some microstructural features, including small dislocation loops and dislocation lines which are highlighted by a slight segregation of Cr. The detected dislocation lines had a total length of 155 nm in a volume of 0.003 um^3, a density of 5.3×10^{-5} nm^{-2}. Five dislocation loops were detected with a mean diameter of 7±4 nm (CI95) and number density of 1.7×10^{21} m^3. This analysis includes 171 Cr-rich clusters which are not obviously associated with dislocations or dislocation loops. The approximate total volume fraction of the microstructural features was 0.2%, 0.8% and 1.0% for the clusters, loops and dislocation lines, respectively. The distribution of solute between these different features was quantified, with background subtraction and overlap solving, by placing spherical volumes around clusters, with a radius equal to the cluster radius, and around dislocation loops, with a radius slightly larger than the observed Cr segregation. The composition around dislocation lines was quantified

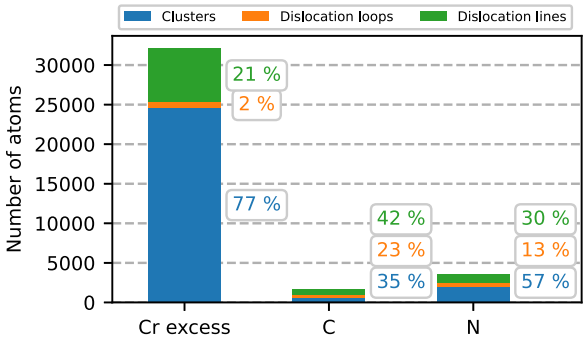

Fig. 14. APT analysis showing the absolute distribution of solute between three microstructural features (clusters, dislocation loops and dislocation lines) in the irradiated Fe-3.28%Cr alloy samples with the presence of carbon and nitrogen. The count of Cr here refers to the excess Cr in these features, whereas for C and N these are the absolute counts. Relative distribution for each element is shown as percentage on the right of corresponding bars.

in a similar manner but using 5 nm radius cylinders oriented along the Cr-segregated regions. A summary of the distribution of the solute in the different microstructural features is shown in Fig. 14. The solute in these features represents 0.4% of all Cr, 6.5% of all C and 10% of all N detected. Of the segregated solute, 77% of Cr was in the clusters and the remainder was primarily in dislocation lines. Because most of the segregated Cr is in the clusters, it is reasonable to assume the Cr behavior in these samples is dominated by the cluster formation. By comparison, less of the segregated C and N is partitioned into the clusters, only 35% and 57% respectively. Therefore Fig. 14 indicates there are differences in the behavior of C and N in this alloy system, specifically that N has a stronger preference to segregate to the Cr-rich clusters than C does.

Another factor which potentially affects the measured C and N composition is the non-detection of multiple hits due to limitations of the delay line detector used in the atom probe technique [69]. To decide if this multiple hit loss is occurring, we can investigate the detected multiple hits for inconsistencies.

In the matrix, 30% of C ions detected are part of multiple hits, but in the clusters multiples comprise 90% of the detected C ions. For nitrogen there is a higher multiples fraction of detected multiples in the matrix (48% are multiples) than the clusters which have a 12% multiple composition. Note that there are approximately ten times as many detected N ions than C ions. For reference there are 9% multiples of Cr in the matrix and 13% in the clusters. Multiple hit loss is more likely where there is a higher fraction of multiples, therefore this evidence points towards likely loss of carbon from the clusters. For nitrogen, the lower multiple fraction in the clusters compared to the matrix may be due to the majority of the matrix-N evaporating from zone-lines and the associated evaporation physics. There is almost 50 times as much N measured at the 110 pole than a non-pole volume, and only 4 times as much C comparing the same volumes. However, the lower measured multiple fraction might indicate that some of the N ions are not detected due to multiple-hit loss. Without further equipment development it is not possible to elaborate further.

In summary, a high number density of small Cr-rich clusters were detected in both Cr concentration materials in both irradiation conditions. These clusters were small (2.9±0.2 nm) with a Cr-fraction of 0.3–0.6, C+N fraction of 0.05 and there is some evidence of loss of C, and to a lesser extent N, from the measured cluster composition.

7. Comparison of simulations with experimental observations

For the analysis of both experimental samples and the Monte Carlo simulations, Maximum Separation Method has been chosen (described elsewhere [70]) to ensure the results are comparable. Since APT does not detect vacancies, only C, N and Cr composition in the clusters and the cluster morphology may be compared.

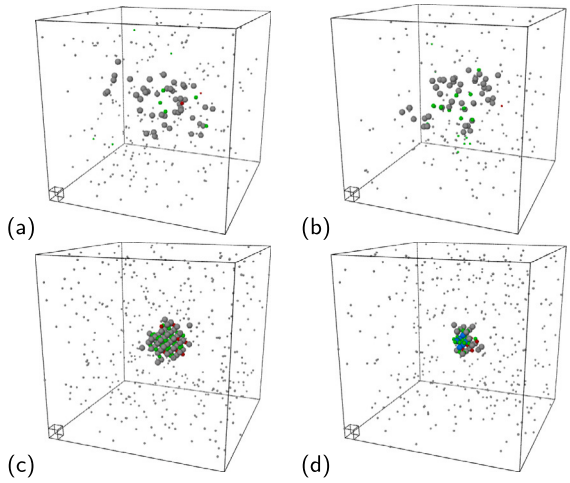

Fig. 15. Visual comparison of example clusters found in (a-b) APT experimental measurements and (c-d) MC simulations. The unit cell of 0.28 nm size is shown in the left near corner of each subfigure. (c) is taken from a simulation without vacancies and Fe-3.28at.%Cr, 0.007at.%C + 0.028at.%N, (d) is taken from Fe-3.28Cr, 0.01at.%Vac, 0.007at.%C + 0.028at.%N.

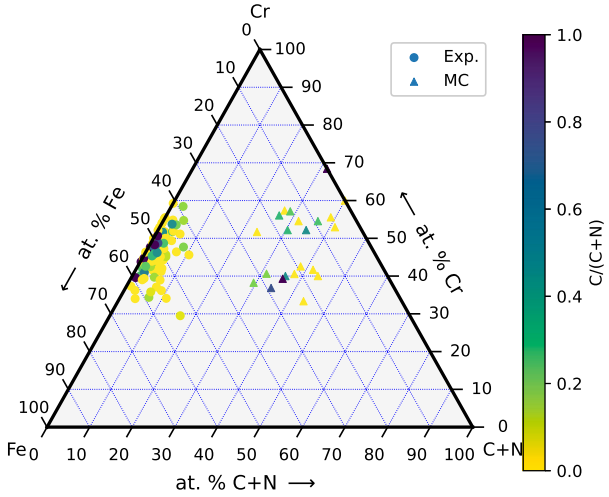

Fig. 16. Relative concentration of Cr,C and N in individual clusters measured experimentally by APT and simulated using MC. Experimental measurements and MC simulations are performed for samples of Fe-3.28at.%Cr with varying low concentrations of defects. The analysis is performed with MSM. MC compositions are 0.007% C, 0.028% N, 0/0.005/0.01% Vac.

It has been shown that there is a variety of observed types of clusters in Fe-Cr-Vac-C-N alloys both in MC simulations (see Fig. 10) and APT measurements (see Fig. 12). More details are given in the supplementary information [65], specifically the distribution of C and N within different-sized clusters, as shown in Fig. S7.

Fig. 15 shows pairs of example clusters from APT observations and MC simulations to illustrate the difference in the structure of clusters between the simulations and observations. As can be seen from Fig. 15, the APT clusters are less dense and larger in size compared to MC clusters: the average size of clusters in APT is 2.9 nm, whereas it is 0.9 nm in MC simulations. This is attributed to the trajectory aberrations that smear the positions of atoms in the directions perpendicular to the evaporation direction. Also, note that the point cloud representation is missing approximately 50% of the atoms due to the limited detection efficiency of the atom probe. Fewer C+N atoms are found inside the clusters in APT compared to MC simulation, which can be partly attributed to detection efficiency and potentially by the multiple-hit loss and migration of C and N in the experiment, whereas all atoms are tracked in the simulations. Both these factors result in the lower solute density of the clusters in APT measurements in comparison with MC simulations. Another important difference is that the structure of MC simulations is not completely representative due to the on-lattice nature, which does not show the changes to the structure caused by the stress fields of the defects.

It should be noted that Monte Carlo simulations produce the atomic arrangement at thermodynamic equilibrium, which may not be fully established in the experimental samples. The experimental measurements are not expected to be at thermal equilibrium due to the short duration (below 9 hours) of the irradiation exposure and the influence of the ion irradiation, which causes additional displacement mixing. As has been discussed in Section 6, the interstitial elements are found not only inside the clusters but also in the close vicinity of the clusters, showing the tendency of Cr and interstitials to aggregate together. It can be hypothesized, that this is the off-thermal equilibrium state, and given enough thermal energy, the interstitials would migrate inside the clusters forming structures similar to ones observed in MC simulations.

A set of MC simulations with the nominal concentrations of defects identical to those in the experimental sample has been performed. Since the vacancy concentration in the experimental samples is not known, only their presence is certain, two additional sets of simulations have been performed with various Vac concentrations (0.005 at.% and 0.01 at.%). The results of these three sets of simulations are compared to the results of experimental measurements in Fig. 16. As can be seen from this figure, the concentration of Cr from both MC simulations and experimental measurements is within the same boundaries. Taking into account the fact that the multiple-hit loss effect does not strongly affect the detection of Cr in the experiments, and the deviation of Cr concentration due to the choice of MSM parameters being smaller than the range of concentrations detected, the correspondence between simulations and experiment is very close. While the Cr concentration is similar, the C and N concentration is lower, which can be explained by the issues raised above, relating to multiple-hit loss, migration, lack of thermal equilibrium and displacement mixing in the experiment.

It should be noted that since vacancies in our simulations are treated as a certain type of atomic species and there is no way for them to disappear from the simulated lattice, the equilibrium is reached when the exchanges of atoms (including Vac) no longer result in significant changes of the free energy, which only fluctuates around its “equilibrium” value. As such, the resulting thermal equilibrium is different to a real thermal equilibrium, where vacancy concentration adjusts to temperature, through either Frenkel pair annihilation of the evaporation of vacancies to sinks and surfaces. This is also another motivation for running sets of MC simulations over a broad range of vacancy concentrations, see Fig. 11. Given that the experimental results for Cr concentration in the clusters are in the range of 30-60%, we are able to set a limit to the Vac concentration, deducing it from the MC simulations themselves, as not exceeding 0.02 at.%.

The presently available MC model does not permit the investigation of line defects, however, it still enables identifying the differences in the cluster structure depending on the local concentration of C, N, and vacancies, as shown in Section 5. The evidence presented in Fig. 14 shows the majority of the excess Cr detected in APT is attributed to cluster features, which gives reasonable confidence in the comparison to the MC modeling which does not include line defects. As identified in Fig. 14, there is a difference in the clustering behavior of C and N with Cr, as well as preferences in this system for the segregation of C and N to different defects.

8. Conclusions

In this work, we formulated and explored a model for Fe-Cr alloys containing vacancies and C/N interstitial atoms, based on a large set of DFT calculations of ordered and disordered phases, with and without defects. Binding energies as well as the stability of ordered phases

both play a role in the resulting atomic structure observed in MC simulations: while Vac-Vac binding is responsible for the formation of vacancy clusters, the binding of Vac-C is weaker than in Vac-N, and the more frequent segregation of C to vacancy clusters is likely caused by dominant segregation of N to Cr clusters, which is in turn caused by the high stability of ordered $[Fe_xCr_y]_3[C_aN_b]$ phases with high N content.

In accord with existing knowledge, MC simulations for systems at 650 K show no precipitation of Cr in Fe-3.28 at.% Cr alloy without non-equilibrium defects as well as in alloys with various concentrations of vacancies, explained by the repulsive nature of Cr-Cr interaction and significantly stronger binding of Vac-Vac compared to Vac-Cr.

With the addition of interstitial C and N, starting at 0.01 at.%, Cr-enriched clusters form in MC simulations. The structure of these Cr-rich precipitates, as well as defect clusters, depends on the local concentration of C, N and vacancies. Overall, a high concentration of vacancies suppresses the formation of Cr-enriched clusters by forming compact Vac-C-N clusters (gas bubbles or graphite precipitations) instead. On the other hand, increased concentration of N and/or C interstitials leads to higher concentration of Cr in the clusters, with nitrogen having on average stronger effect on such an increase of Cr compared to carbon.

APT measurements performed using two alloy samples provide a qualitatively similar picture of Cr segregating into clusters with increased concentration of C and N in them and in their vicinity. The Cr-N-C rich clusters identified by APT are strikingly similar to those predicted by MC, being of somewhat similar size, number density and composition. Analysis of APT results also enabled the identification of other microstructural features attracting Cr, namely dislocation lines and dislocation loops, however, in smaller amount compared to clusters.

The qualitative agreement between MC simulations and APT measurements for the concentration of Cr in the clusters gives credibility to the mechanisms of Cr clustering proposed in this study. The and observed results explain the anomalous Cr clustering in a low Cr-content Fe-Cr alloy and highlight the importance of, even very small quantities of C and N, in this technologically important alloy system.

CRediT authorship contribution statement

Mark Fedorov: Data curation, Methodology, Software, Validation, Visualization, Writing – original draft, Writing – review & editing. **Jan S. Wróbel:** Conceptualization, Funding acquisition, Methodology, Resources, Writing – original draft, Writing – review & editing. **Andrew J. London:** Data curation, Funding acquisition, Investigation, Methodology, Validation, Visualization, Writing – original draft, Writing – review & editing. **Krzysztof J. Kurzydłowski:** Writing – review & editing. **Chu-Chun Fu:** Writing – review & editing. **Tonči Tadić:** Resources. **Sergei L. Dudarev:** Funding acquisition, Writing – review & editing. **Duc Nguyen-Manh:** Conceptualization, Funding acquisition, Supervision, Writing – original draft, Writing – review & editing.

Declaration of competing interest

The authors declare that they have no known competing financial interests or personal relationships that could have appeared to influence the work reported in this paper.

Data availability

Data will be made available on request.

Acknowledgements

This work has been carried out within the framework of the EUROfusion Consortium, funded by the European Union via the Euratom Research and Training Programme (Grant Agreement No 101052200 — EUROfusion) and was partially supported by the Broader Approach Phase II agreement under the PA of IFERC2-T2PA02. Views and opinions expressed are however those of the author(s) only and do not necessarily reflect those of the European Union or the European Commission. Neither the European Union nor the European Commission can be held responsible for them. The research used UKAEA's Materials Research Facility, which has been funded by and is a part of the UK National Nuclear User Facility and Henry Royce Institute for Advanced Materials. AJL, SLD and DNM acknowledge funding from the RCUK Energy Programme Grant No. EP/W006839/1. The work at WUT has been carried out as a part of an international project co-financed by the Polish Minister of Science and Higher Education through the PMW program in 2022; Agreement No. 5257/HEU-EURATOM/2022/2. JSW, MF and DNM would like to acknowledge the use of high-performance computing facility MARCONI (Bologna, Italy) provided by EUROfusion.

Appendix A. Supplementary material

Supplementary material related to this article can be found online at https://doi.org/10.1016/j.jnucmat.2023.154715.

References

[1] D. Stork, P. Agostini, J.-L. Boutard, D. Buckthorpe, E. Diegele, S.L. Dudarev, C. English, G. Federici, M.R. Gilbert, S. Gonzalez, A. Ibarra, C. Linsmeier, A.L. Puma, G. Marbach, L.W. Packer, B. Raj, M. Rieth, M.Q. Tran, D.J. Ward, S.J. Zinkle, Materials R&D for a timely DEMO: key findings and recommendations of the EU Roadmap Materials Assessment Group, Fusion Eng. Des. 89 (7) (2014) 1586–1594.

[2] R. Lindau, A. Möslang, M. Schirra, Thermal and mechanical behaviour of the reduced-activation-ferritic-martensitic steel EUROFER, Fusion Eng. Des. 61–62 (2002) 659–664.

[3] E. Lucon, P. Benoit, P. Jacquet, E. Diegele, R. Lässer, A. Alamo, R. Coppola, F. Gillemot, P. Jung, A. Lind, S. Messoloras, P. Novosad, R. Lindau, D. Preininger, M. Klimiankou, C. Petersen, M. Rieth, E. Materna-Morris, H.-C. Schneider, J.-W. Rensman, B. van der Schaaf, B.K. Singh, P. Spaetig, The European effort towards the development of a demo structural material: irradiation behaviour of the European reference RAFM steel EUROFER, Fusion Eng. Des. 81 (8) (2006) 917–923.

[4] C.D. Hardie, C.A. Williams, S. Xu, S.G. Roberts, Effects of irradiation temperature and dose rate on the mechanical properties of self-ion implanted Fe and Fe–Cr alloys, J. Nucl. Mater. 439 (1–3) (2013) 33–40.

[5] J.C. Haley, S. de Moraes Shubeita, P. Wady, A.J. London, G.R. Odette, S. Lozano-Perez, S.G. Roberts, Microstructural examination of neutron, proton and self-ion irradiation damage in a model Fe9Cr alloy, J. Nucl. Mater. 533 (2020) 152130.

[6] S. Hari Babu, R. Rajaraman, G. Amarendra, R. Govindaraj, N.P. Lalla, A. Dasgupta, G. Bhalerao, C.S. Sundar, Dislocation driven chromium precipitation in Fe-9Cr binary alloy: a positron lifetime study, Philos. Mag. 92 (23) (2012) 2848–2859.

[7] V. Kuksenko, C. Pareige, P. Pareige, Cr precipitation in neutron irradiated industrial purity Fe-Cr model alloys, J. Nucl. Mater. 432 (1–3) (2013) 160–165.

[8] W. Xiong, M. Selleby, Q. Chen, J. Odqvist, Y. Du, Phase equilibria and thermodynamic properties in the Fe-Cr system, Crit. Rev. Solid State Mater. Sci. 35 (2) (2010) 125–152.

[9] Z. Jiao, G.S. Was, Segregation behavior in proton- and heavy-ion-irradiated ferritic-martensitic alloys, Acta Mater. 59 (11) (2011) 4467–4481.

[10] P.M. Derlet, S.L. Dudarev, Microscopic structure of a heavily irradiated material, Phys. Rev. Mater. 4 (2) (2020) 023605.

[11] M.J. Swenson, J.P. Wharry, Nanocluster irradiation evolution in Fe-9%Cr ODS and ferritic-martensitic alloys, J. Nucl. Mater. 496 (2017) 24–40.

[12] M. Bachhav, G.R. Odette, E.A. Marquis, Microstructural changes in a neutron-irradiated Fe-15 at.%Cr alloy, J. Nucl. Mater. 454 (1) (2014) 381–386.

[13] M. Bachhav, G.R. Odette, E.A. Marquis, α' precipitation in neutron-irradiated Fe-Cr alloys, Scr. Mater. 74 (2014) 48–51.

[14] C. Domain, C.S. Becquart, J. Foct, Ab initio study of foreign interstitial atom (C, N) interactions with intrinsic point defects in α-Fe, Phys. Rev. B 69 (14) (2004) 144112.

[15] C.J. Först, J. Slycke, K.J. Van Vliet, S. Yip, Point defect concentrations in metastable Fe-C alloys, Phys. Rev. Lett. 96 (2006) 175501.

[16] T. Jourdan, C.-C. Fu, L. Joly, J.L. Bocquet, M.J. Caturla, F. Willaime, Direct simulation of resistivity recovery experiments in carbon-doped α-iron, Phys. Scr. T 145 (2011) 014049.

[17] C. Barouh, T. Schuler, C.-C. Fu, M. Nastar, Interaction between vacancies and interstitial solutes (C, N, and O) in α-Fe: from electronic structure to thermodynamics, Phys. Rev. B 90 (5) (2014) 054112.

[18] M.Yu. Lavrentiev, D. Nguyen-Manh, S.L. Dudarev, Chromium-vacancy clusters in dilute bcc Fe-Cr alloys: an ab initio study, J. Nucl. Mater. 499 (2018) 613–621.

[19] G. Bonny, A. Bakaev, D. Terentyev, Energetic stability of vacancy-carbon clusters in solid solution alloys: the Fe-Cr-C Case, Phys. Status Solidi B 256 (11) (2019) 1900130.

[20] O. Senninger, F. Soisson, E. Martinez, M. Nastar, C.-C. Fu, Y. Brechet, Modeling radiation induced segregation in iron-chromium alloys, Acta Mater. 103 (2016) 1–11.
[21] R. Herschberg, C.-C. Fu, M. Nastar, F. Soisson, Atomistic modelling of the diffusion of C in Fe–Cr alloys, Acta Mater. 165 (2019) 638–653.
[22] M. Chiapetto, L. Malerba, A. Puype, C.S. Becquart, Object kinetic Monte Carlo study of the effect of grain boundaries in martensitic Fe–Cr–C alloys, Phys. Status Solidi A 213 (11) (2016) 2981–2987.
[23] J.S. Wróbel, D. Nguyen-Manh, K.J. Kurzydłowski, S.L. Dudarev, A first-principles model for anomalous segregation in dilute ternary tungsten-rhenium-vacancy alloys, J. Phys. Condens. Matter 29 (14) (2017) 145403.
[24] D. Nguyen-Manh, J.S. Wróbel, M. Klimenkov, M.J. Lloyd, L. Messina, S.L. Dudarev, First-principles model for voids decorated by transmutation solutes: short-range order effects and application to neutron irradiated tungsten, Phys. Rev. Mater. 5 (2021) 065401.
[25] N. Saunders, A.P. Miodownik, CALPHAD (Calculation of Phase Diagrams): A Comprehensive Guide, vol. 1, Pergamon, 1998.
[26] M. Hillert, Phase Equilibria, Phase Diagrams and Phase Transformations: Their Thermodynamic Basis, 2 edition, Cambridge University Press, 2007.
[27] C. Guéneau, N. Dupin, L. Kjellqvist, E. Geiger, M. Kurata, S. Gossé, E. Corcoran, A. Quaini, R. Hania, A.L. Smith, M.H.A. Piro, T. Besmann, P.E.A. Turchi, J.C. Dumas, M.J. Welland, T. Ogata, B.O. Lee, J.R. Kennedy, C. Adkins, M. Bankhead, D. Costa, TAF-ID: an international thermodynamic database for nuclear fuels applications, Calphad 72 (2021) 102212.
[28] Cláudio G. Schön, Matheus A. Tunes, Raymundo Arróyave, John Ågren, On the complexity of solid-state diffusion in highly concentrated alloys and the sluggish diffusion core-effect, Calphad 68 (2020) 101713.
[29] A. Obaied, F. Tang, I. Roslyakova, M. to Baben, “2 1/2th” generation Calphad databases: extrapolating heat capacities of elements and compounds to 0 K, Calphad 75 (2021) 102352.
[30] Aurélie Jacob, Erwin Povoden-Karadeniz, Philipp Retzl, Ernst Kozeschnik, Reassessment of low-temperature Gibbs energies of BCC and FCC in steel for T0-temperature evaluation, Calphad 81 (2023) 102531.
[31] Sedigheh Bigdeli, Li-Fang Zhu, Albert Glensk, Blazej Grabowski, Bonnie Lindahl, Tilmann Hickel, Malin Selleby, An insight into using DFT data for calphad modeling of solid phases in the third generation of Calphad databases, a case study for al, Calphad 65 (2019) 79–85.
[32] Yimi Wang, Kangming Li, Frédéric Soisson, Charlotte S. Becquart, Combining DFT and Calphad for the development of on-lattice interaction models: the case of Fe-Ni system, Phys. Rev. Mater. 4 (2020) 113801.
[33] Guillaume Deffrennes, Benoit Oudot, A self-consistent model to describe the temperature dependence of the bulk modulus, thermal expansion and molar volume compatible with 3rd generation Calphad databases, Calphad 74 (2021) 102291.
[34] D.E. Jiang, Emily A. Carter, Carbon dissolution and diffusion in ferrite and austenite from first principles, Phys. Rev. B 67 (2003) 214103.
[35] Wei Xiong, Malin Selleby, Qing Chen, Joakim Odqvist, Yong Du, Phase equilibria and thermodynamic properties in the Fe-Cr system, Crit. Rev. Solid State Mater. Sci. 35 (2) (2010) 125–152.
[36] O. Buggenhoudt, Modelling and simulation of carbides in alpha-Fe alloys from first principles: alloying elements, diffusion and nucleation, PhD thesis, Université Paris-Saclay, 2021.
[37] G. Kresse, J. Hafner, Ab initio molecular dynamics for liquid metals, Phys. Rev. B 47 (1) (1993) 558–561.
[38] G. Kresse, J. Hafner, Ab initio molecular-dynamics simulation of the liquid-metal–amorphous-semiconductor transition in germanium, Phys. Rev. B 49 (20) (1994) 14251–14269.
[39] G. Kresse, J. Furthmüller, Efficiency of ab-initio total energy calculations for metals and semiconductors using a plane-wave basis set, Comput. Mater. Sci. 6 (1) (1996) 15–50.
[40] G. Kresse, J. Furthmüller, Efficient iterative schemes for ab initio total-energy calculations using a plane-wave basis set, Phys. Rev. B 54 (16) (1996) 11169–11186.
[41] P.E. Blöchl, Projector augmented-wave method, Phys. Rev. B 50 (24) (1994) 17953–17979.
[42] G. Kresse, D. Joubert, From ultrasoft pseudopotentials to the projector augmented-wave method, Phys. Rev. B 59 (3) (1999) 1758–1775.
[43] J.P. Perdew, K. Burke, M. Ernzerhof, Generalized gradient approximation made simple, Phys. Rev. Lett. 77 (18) (1996) 3865–3868.
[44] J.D. Pack, H.J. Monkhorst, Special points for Brillouin-zone integrations, Phys. Rev. B 13 (12) (1976) 5188–5192.
[45] A. van de Walle, G. Ceder, Automating first-principles phase diagram calculations, J. Phase Equilib. 23 (4) (2002) 348–359.
[46] A. van de Walle, M. Asta, Self-driven lattice-model Monte Carlo simulations of alloy thermodynamic properties and phase diagrams, Model. Simul. Mater. Sci. Eng. A 10 (5) (2002) 521–538.
[47] A. van de Walle, Multicomponent multisublattice alloys, nonconfigurational entropy and other additions to the Alloy Theoretic Automated Toolkit, Calphad 33 (2) (2009) 266–278.
[48] G.L.W. Hart, R.W. Forcade, Algorithm for generating derivative structures, Phys. Rev. B 77 (22) (2008) 224115.
[49] J. Le Coze, Procurement of pure Fe metal and Fe-based alloys with controlled chemical alloying element contents and microstructure, in: ARMINES Ecole Nationale Superieure des Mines, 2007.
[50] C.D. Hardie, A.J. London, J.J.H. Lim, R. Bamber, T. Tadić, M. Vukšić, S. Fazinić, Exploitation of thermal gradients for investigation of irradiation temperature effects with charged particles, Sci. Rep. 9 (2019) 13541.
[51] M.K. Miller, K.F. Russell, K. Thompson, R. Alvis, D.J. Larson, Review of atom probe FIB-based specimen preparation methods, Microsc. Microanal. 13 (6) (2007) 428–436.
[52] T.C. Kunicki, D. Beermann, B.G. Geiser, E. Oltman, R.W. O’Neill, D.J. Larson, Atom probe data reconstruction, visualization and analysis with the imago visualization and analysis system (IVAS¿), in: 2006 19th International Vacuum Nanoelectronics Conference, IEEE, July 2006.
[53] 3depict - visualisation & analysis for atom probe, online, accessed: 12-April-2019.
[54] J.M. Hyde, C.A. English, Microstructural processes in irradiated materials, in: MRS 2000 Fall Meet, Symp, Boston, MA, 2001, pp. 27–29.
[55] L.T. Stephenson, M.P. Moody, P.V. Liddicoat, S.P. Ringer, S. Byers, A.E. Rafferty, A. Cerezo, L. Davin, P.J. Clark, F.C. Evans, et al., New techniques for the analysis of fine-scaled clustering phenomena within atom probe tomography (APT) data, Microsc. Microanal. 13 (6) (2007) 448–463.
[56] C.A. Williams, D. Haley, E.A. Marquis, G.D.W. Smith, M.P. Moody, Defining clusters in APT reconstructions of ODS steels, Ultramicroscopy 132 (2013) 271–278.
[57] M. Yu Lavrentiev, R. Drautz, D. Nguyen-Manh, T.P.C. Klaver, S.L. Dudarev Monte, Carlo study of thermodynamic properties and clustering in the bcc Fe-Cr system, Phys. Rev. B 75 (1) (2007) 014208.
[58] J.S. Wróbel, D. Nguyen-Manh, M.Yu. Lavrentiev, M. Muzyk, S.L. Dudarev, Phase stability of ternary fcc and bcc Fe-Cr-Ni alloys, Phys. Rev. B 91 (2015) 024108.
[59] C. Domain, C.S. Becquart, Ab initio calculations of defects in Fe and dilute Fe-Cu alloys, Phys. Rev. B 65 (2001) 024103.
[60] A. Bakaev, D. Terentyev, X. He, E.E. Zhurkin, D. Van Neck, Interaction of carbon-vacancy complex with minor alloying elements of ferritic steels, J. Nucl. Mater. 451 (1–3) (2014) 82–87.
[61] A.T. Paxton, C. Elsässer, Analysis of a carbon dimer bound to a vacancy in iron using density functional theory and a tight binding model, Phys. Rev. B 87 (2013) 224110.
[62] Timothy T. Lau, Clemens J. Först, Xi Lin, Julian D. Gale, Sidney Yip, Krystyn J. Van Vliet, Many-body potential for point defect clusters in Fe-C alloys, Phys. Rev. Lett. 98 (2007) 215501.
[63] G. Bonny, R.C. Pasianot, L. Malerba, A. Caro, P. Olsson, M.Yu. Lavrentiev, Numerical prediction of thermodynamic properties of iron-chromium alloys using semi-empirical cohesive models: the state of the art, J. Nucl. Mater. 385 (2) (2009) 268–277.
[64] D.R. Mason, F. Granberg, M. Boleininger, T. Schwarz-Selinger, K. Nordlund, S.L. Dudarev, Parameter-free quantitative simulation of high-dose microstructure and hydrogen retention in ion-irradiated tungsten, Phys. Rev. Mater. 5 (2021) 095403.
[65] See supplemental material for additional information not fit for the main part of the manuscript, including the intermediate data from cluster expansion and a more detailed analysis of defect clusters.
[66] G.S. Was, S. Taller, Z. Jiao, A.M. Monterrosa, D. Woodley, D. Jennings, T. Kubley, F. Naab, O. Toader, E. Uberseder, Resolution of the carbon contamination problem in ion irradiation experiments, Nucl. Instrum. Methods Phys. Res. B 412 (2017) 58–65.
[67] A.J. London, S. Lozano-Perez, M.P. Moody, S. Amirthapandian, B.K. Panigrahi, C.S. Sundar, C.R.M. Grovenor, Quantification of oxide particle composition in model oxide dispersion strengthened steel alloys, Ultramicroscopy 159 (2015) 360–367.
[68] B. Gault, F. Danoix, K. Hoummada, D. Mangelinck, H. Leitner, Impact of directional walk on atom probe microanalysis, Ultramicroscopy 113 (2012) 182–191.
[69] M. Thuvander, A. Kvist, L.J.S. Johnson, J. Weidow, H.-O. Andrén, Reduction of multiple hits in atom probe tomography, Ultramicroscopy 132 (2013) 81–85.
[70] E.A. Jägle, P.-P. Choi, D. Raabe, The maximum separation cluster analysis algorithm for atom-probe tomography: parameter determination and accuracy, Microsc. Microanal. 20 (6) (2014) 1662–1671.